2015

Electronic properties of chiral two-dimensional materials

Christopher Lawrence Charles Triola
College of William & Mary - Arts & Sciences

Electronic Properties of Chiral Two-Dimensional Materials

Christopher Lawrence Charles Triola

Fredericksburg, Virginia

Master of Science, College of William and Mary, 2011
Bachelor of Science, University of Mary Washington, 2009

A Dissertation presented to the Graduate Faculty
of the College of William and Mary in Candidacy for the Degree of
Doctor of Philosophy

Department of Physics

The College of William and Mary
May 2015

APPROVAL PAGE

This Dissertation is submitted in partial fulfillment of
the requirements for the degree of

Doctor of Philosophy

Christopher Lawrence Charles Triola

Approved by the Committee, February, 2015

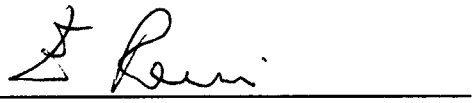

Committee Chair
Assistant Professor Enrico Rossi, Physics
The College of William and Mary

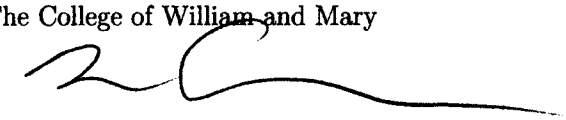

Professor Marc Sher, Physics
The College of William and Mary

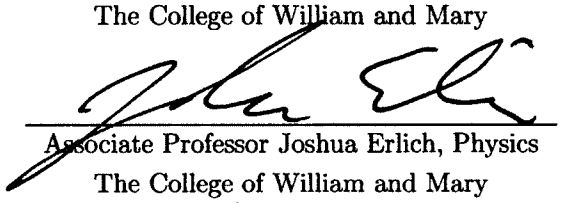

Associate Professor Joshua Erlich, Physics
The College of William and Mary

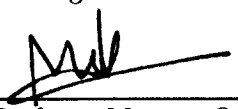

Assistant Professor Mumtaz Qazilbash, Physics
The College of William and Mary

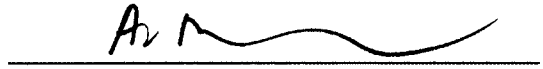

Dr. Alexander Balatsky, Physics
Los Alamos National Laboratory/NORDITA

ABSTRACT

In this dissertation we study the electronic properties of certain two-dimensional chiral electron systems. We study the static and dynamic screening of gapped bilayer graphene and find important qualitative differences between the dielectric screening function obtained using a simplified 2-band model and that obtained using a more sophisticated 4-band model. We also formulate a continuum model to study the low-energy electronic properties of heterostructures formed by graphene on a strong three-dimensional topological insulator (TI) both for the case of commensurate and incommensurate stacking. We find that the proximity of the TI induces a strong enhancement of the spin-orbit coupling in graphene that can be tuned via the twist angle. Additionally, we examine the effect of a spin-active interface on the symmetry of proximity-induced superconducting pairing amplitudes in topological insulators. We compare our results to those for normal metals and ferromagnetic materials finding that the nontrivial spin chirality of the TI leads to qualitatively different behavior of the pairing amplitude. Lastly, we study the many-body instabilities of the Dirac states predicted to arise on the surfaces of topological Kondo insulators identifying regions of parameter space in which the system exhibits spin density wave, and charge density wave order.

TABLE OF CONTENTS

Acknowledgments iii

Dedication iv

List of Tables v

List of Figures vi

CHAPTER

1 Introduction 2

2 Model Hamiltonians for Two-Dimensional Chiral Electron Systems 5

2.1 Graphene 7

2.1.1 Single Layer Graphene: A Two-Dimensional Dirac Material . . . 7

2.1.2 Bilayer Graphene: A Novel Chiral Hamiltonian 13

2.2 Topological Insulators 17

3 Screening and Collective Modes in Gapped Bilayer Graphene 23

3.1 Model 25

3.2 Polarizability and Dielectric Function 26

3.3 Summary 34

4 Proximity Effect in Graphene-Topological Insulator Heterostructures 36

4.1 Basic Considerations 38

4.2 Commensurate Stacking 39

4.3 Incommensurate Stacking 44

4.4 Summary 48

5 Effect of a Spin-Active Interface on Proximity-Induced Superconductivity . . 49

5.1 Model and Setup 51

5.2 Proximity-Induced Pairing 53

5.3 Summary 58

6 Many-body instabilities and mass generation in slow Dirac materials 60

6.1 Theoretical Model and Methods 62

6.2 Numerical Results and Discussion 66

6.3 Summary 71

7 Conclusion 72

APPENDIX A
Supercell Technique 74

Bibliography 77

Vita 90

ACKNOWLEDGMENTS

Firstly, I thank my advisor, Enrico Rossi, for taking me as a student, providing me with good projects, offering constructive feedback on every project, and helping me to develop as a physicist. Also, I thank Marc Sher, who helped me decide to attend the College of William and Mary, introduced me to Enrico, and provided wisdom in times of need. I thank Alexander (Sasha) Balatsky for taking me as a summer student at Los Alamos National Laboratory and helping me discover new areas of physics to which I would not otherwise have been exposed. I express my thanks also to my colleagues: Junhua Zhang, Martin Alexander Rodriguez-Vega, Johannes (Satrio) Gani, Yudistira Virgus, Christopher Hendriks, and Gardner Marshall for incredibly useful conversations when I was stuck on problems and general moral support throughout my research experience. Last but not least, I express my deepest gratitude to my sisters, Lauren and Shannon, and my parents Mary and Larry Triola for encouraging me to pursue an advanced degree in physics and putting up with me throughout my brief existence.

Dedicated to Eru Ilúvatar, creator of Eä and keeper of the secret fire.

LIST OF TABLES

5.1 Comparison of Proximity-Induced Pairing in TI|SC, N|SC, FZ|SC, and FE|SC 57

LIST OF FIGURES

2.1 Three different examples of chirality. 6

2.2 Single layer graphene. 8

2.3 Energy bands for single layer graphene over full Brillouin zone. 11

2.4 Bernal stacked bilayer graphene lattice with hopping parameters γ_1, and γ_3 labeled. 13

2.5 Energy bands for bilayer graphene. 16

3.1 Static polarizability, band structure, and chirality factors for bilayer graphene. 28

3.2 Fermi surface and polarizability for gapped bilayer graphene with trigonal warping. 30

3.3 RPA dielectric function for gapped bilayer graphene. 31

3.4 RPA dielectric function for bilayer graphene with trigonal warping. 32

3.5 Long wavelength plasmon dispersion for gapped bilayer graphene. 34

4.1 Schematic of stacked graphene-topological insulator heterostructure and electronic structure for commensurate stacking. 41

4.2 Schematic of incommensurate stacked graphene-topological insulator heterostructure. 43

4.3 Electronic structure for incommensurate stacked graphene-topological insulator heterostructure. Splitting of the bands can be tuned with relative twist angle. 46

4.4 Induced spin texture in incommensurate stacked graphene-topological insulator heterostructure considering a single Fermi pocket. 48

5.1 Schematic of topological insulator-superconductor heterostructure. 51

6.1 Band structure for model of topological Kondo insulator. 63

6.2 Phase diagram for topological Kondo insulator with repulsive on-site interaction. 67

6.3 Charge density wave solution. 68

6.4 Phase diagram for topological Kondo insulator with attractive on-site interaction. 68

ELECTRONIC PROPERTIES OF CHIRAL TWO-DIMENSIONAL MATERIALS

CHAPTER 1

Introduction

The archetypal instance of a two-dimensional fermionic system in condensed matter is the two-dimensional electron gas (2DEG). As the name would suggest, this is a system which behaves as an ensemble of non-interacting fermions confined to a two-dimensional plane, typically having the familiar parabolic energy-momentum relation, $E_{\mathbf{p}} = \mathbf{p}^2/2m^*$, except with an effective mass m^* usually differing from the free electron mass, m_e. 2DEGs can be found in a variety of solid state systems including at the 111 surface of Cu, confined to the surface of liquid He, and in Metal-Oxide-Semiconductor structures [1]. Much of the behavior of the electrons comprising a 2DEG has been thoroughly studied and many interesting results have appeared in the literature [1]. However, there are a number of systems in which the low energy fermionic excitations possess a spin-like degree of freedom that exhibits a nontrivial texture in momentum space. In these chiral systems the interplay between momentum and spin degrees of freedom can lead to a number of interesting deviations from the behavior of standard non-chiral 2DEGs. In this dissertation we will consider three distinct types of chiral 2DEGs and explore some of their electronic properties. We will also consider the electronic properties of heterostructures composed of these chiral

materials.

In Chapter 2 we discuss the sense in which graphene, bilayer graphene, and topological insulators exhibit "chiral" two-dimensional electronic states and explain the origin of the chirality manifested in each system. Furthermore, we introduce the model Hamiltonians used in subsequent chapters to investigate the properties of chiral two-dimensional systems.

In Chapter 3 we study the static and dynamic screening of gapped bilayer graphene using the models discussed in Chapter 2. We compare results obtained using a robust 4-band model to results from the literature which were obtained using a simplified 2-band model. We find important qualitative differences between the dielectric screening function obtained using the two models. In particular within the 4-band model in the presence of a band-gap the static screening exhibits Kohn anomalies that are absent within the 2-band model. We also find that the plasmon modes have qualitatively different character in the 4-band model compared to 2-band results. Additionally, we characterize the effect of trigonal warping on the screening properties of bilayer graphene.

In Chapter 4 we formulate a continuum model to study the low-energy electronic states of heterostructures formed by graphene on a strong three-dimensional topological insulator (TI) both for the case of commensurate and incommensurate stacking of the two lattices. The incommensurability can be due to a twist angle between graphene and the TI surface, or a lattice mismatch between the two systems. We find that the proximity of the TI enhances the spin-orbit coupling in the graphene and that this effect can be tuned via the twist angle.

In Chapter 5 we examine the effect of a spin-active interface on the symmetry of proximity-induced superconducting pairing amplitudes in topological insulators. We develop a model to investigate the leading order contribution to the pairing amplitude considering three different kinds of spin-active interfaces: (i) those that induce spin-dependent scattering phases, (ii) those that flip the spin of incident electrons, and (iii) interfaces that

both induce spin-dependent phases and flip the spins of incident electrons. We find that in cases (i) and (iii) odd-frequency triplet pairing is induced in the TI while for case (ii) no odd-frequency pairing is induced to leading order. We compare our results to those for normal metals and ferromagnetic materials finding that the nontrivial spin chirality of the TI leads to qualitatively different behavior.

In Chapter 6, we introduce a tight-binding model for studying the surface states of topological Kondo insulators. We study the relationship between the model parameters and characteristics of the surface band structure then use mean-field theory to study the many-body instabilities of these systems. Regions of parameter space are identified in which the system exhibits spin density wave, and charge density wave order.

CHAPTER 2

Model Hamiltonians for Two-Dimensional Chiral Electron Systems

As noted in Chapter 1, some condensed matter systems can be well-described by an effective Hamiltonian whose eigenstates, $|\psi_{\mathbf{k}}\rangle$, possess a spin-like degree of freedom, $\mathbf{S}$, such that the expectation values of its components, $\langle S_i \rangle = \langle \psi_{\mathbf{k}} | \hat{S}_i | \psi_{\mathbf{k}} \rangle$, depend on the direction of the momentum, $\mathbf{k}$, in a nontrivial way. We refer to such states as "chiral". Chiral states can emerge in a number of different contexts in condensed matter systems, with the spin degree of freedom winding in different ways around the fermi surface as shown in Fig. 2.1. Furthermore, the chiral spin degree of freedom need not be the real electron spin, as we will see in the case of graphene-based materials. One unifying class of materials which includes, as a subset, many chiral materials is the set of Dirac materials, whose quasiparticles are better described as massless Dirac fermions. This class includes graphene, and the surface states of topological insulators [2–6]. In these Dirac materials the

kinetic energy is proportional to the momentum, vp, just like massless relativistic particles but with a speed v that depends on the details of the system. For example, in graphene $v \approx 10^6$m/s$\approx c/300$. The fact that quasiparticles obey the Dirac equation instead of the Schrödinger equation can affect a variety of electronic properties, for example, the integer quantum Hall effect and localization [2, 3, 7, 8].

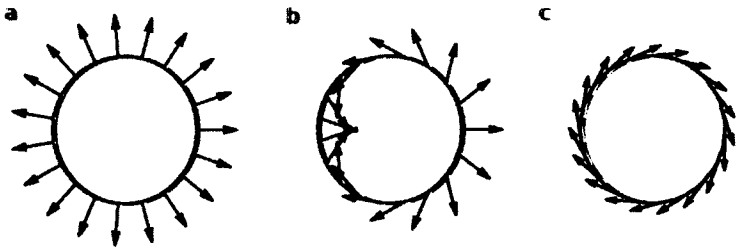

FIG. 2.1: Three different examples of chirality. Each point on the circle represents a direction in momentum space while the arrows represent the direction of a spin, or pseudospin, degree of freedom. (a) Chirality of single layer graphene in the K valley with pseudospin aligned (or anti-aligned) with the direction of momentum. (b) Chirality found in bilayer graphene with pseudospin winding twice around the Fermi surface. (c) Chirality found in topological insulators with spin perpendicular to the direction of momentum.

Dirac materials are not alone in having nontrivial chirality. Multiple layers of graphene can be stacked in such a way to give rise to a number of different unique chiralities [8]. In the following sections we will discuss three materials: graphene, bilayer graphene, and topological insulators. In each case we will present the Hamiltonian(s) used to model their behavior and discuss the kind of chirality exhibited by the system. In subsequent chapters we will use these Hamiltonians to examine the electronic properties of these materials and their heterostructures.

2.1 Graphene

No discussion of chiral two-dimensional materials could begin without mentioning graphene, a one-atom-thick sheet of carbon atoms arranged in a honeycomb lattice. With an extraordinarily high room temperature mobility, high volumetric area to mass ratio, incredible tensile strength, and numerous other superlative properties, graphene has attracted a great deal of attention since its isolation in 2005 [8–11]. In this dissertation our focus will be on graphene's electronic properties, specifically, on the chiral Dirac electron states it hosts at special k-points in its Brillouin zone. Interestingly, when multiple sheets of graphene are stacked appropriately, the low energy electronic states of these systems appear to possess their own unique chirality. One example of a chiral graphene multilayer is A-B stacked bilayer graphene. This system shows great promise for applications in electronics since a gap can be opened and tuned by applying an electric field perpendicular to the two layers [12–17]. In this dissertation we will focus on monolayer and bilayer graphene.

2.1.1 Single Layer Graphene: A Two-Dimensional Dirac Material

Single layer graphene is a one-atom-thick allotrope of carbon arranged in a honeycomb structure [8]. Isolated carbon atoms possess six electrons, one pair fill the $1s^2$ shell, with the remaining four occupying the $2s$ and $2p$ shells. These electrons can hybridize in several different configurations leading to flexible bonds, giving rise to all of organic chemistry and, ultimately, life itself [8, 18, 19]. In graphene, the pair of electrons in the $1s^2$ state remain bound to each carbon atom and do not participate in the electron dynamics of the material at large. However, from the remaining four electrons, one s-electron and two p-electrons hybridize, sp^2 hybridization, creating three σ bonds 120° apart and in the same

plane [8, 19]. The electrons participating in the σ bonds in graphene give rise to a filled valence band and aside from the strength of the graphene lattice do not participate in the electron dynamics. With the $1s^2$ and sp^2 states fixed in relatively inert configurations the only remaining electronic states are the single p_z electrons associated with each carbon atom, where z is the direction perpendicular to the plane formed by the sp^2 hybridized bonds and hence the plane of the graphene. These residual p_z states hybridize with their neighbors to create the filled π band and unfilled π^* band. It is at the intersection of these two bands, π and π^*, that an effective Dirac Hamiltonian emerges. The dynamics of these electrons can be described remarkably well by a tight-binding model, as confirmed by band structure calculations and most experiments [8, 18]. While this picture appears to be consistent with most experiments there is still much work devoted to many-body effects in graphene and other Dirac materials, as we will discuss in Chapter 6. We will now proceed by presenting the tight-binding model for monolayer graphene and from this derive the Dirac Hamiltonian which approximates it at the K and K' points in the Brillouin zone.

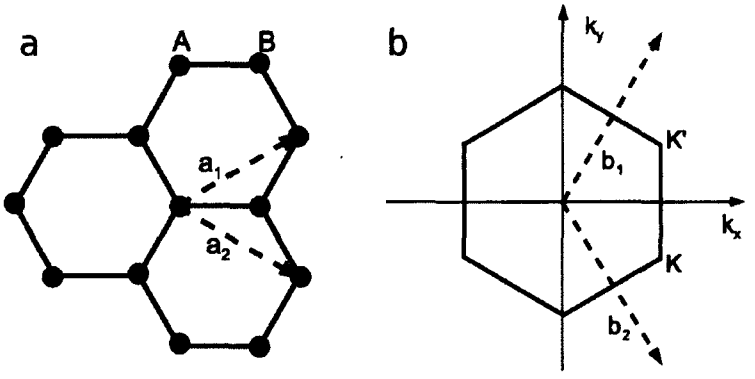

FIG. 2.2: Single layer graphene. (a) Direct lattice for single layer graphene with sublattices, A and B, and primitive vectors $\mathbf{a}_1$ and $\mathbf{a}_2$ labeled. (b) Sketch of the Brillouin zone for graphene with reciprocal primitive lattice vectors $\mathbf{b}_1$ and $\mathbf{b}_2$ and K, K' points labeled.

Before we present the Hamiltonian for graphene, it will be beneficial to make the geometry of the lattice structure more explicit. Graphene is arranged in a honeycomb

lattice which, mathematically, we describe as a triangular Bravais lattice in which the unit cell contains two carbon atoms which we denote A and B, see Fig. 2.2. This sublattice degree of freedom is what gives rise to many of graphene's unique electronic properties. To define any two-dimensional Bravais lattice one must specify the two primitive vectors which generate it and the basis vectors defining the structure within the unit cell. For concreteness we choose the primitive vectors and basis vectors to be

$$\begin{gathered} \mathbf{a}_1 = a\sqrt{3}\left(\frac{\sqrt{3}}{2}\hat{x} + \frac{1}{2}\hat{y}\right);\ \mathbf{a}_2 = a\sqrt{3}\left(\frac{\sqrt{3}}{2}\hat{x} - \frac{1}{2}\hat{y}\right) \\ \mathbf{d}_A = 0;\ \mathbf{d}_B = a\hat{x} \end{gathered} \tag{2.1}$$

where $\mathbf{a}_i$ is a primitive vector, $\mathbf{d}_\alpha$ is the basis vector for sublattice α, and $a = 1.42$ Å denotes the carbon-carbon distance. With the direct lattice defined according to the conventions in Eq 2.1 we can write the reciprocal lattice as a triangular Bravais lattice generated by the reciprocal primitive lattice vectors:

$$\begin{aligned} \mathbf{b}_1 &= \frac{4\pi}{3a}\left(\frac{1}{2}\hat{x} + \frac{\sqrt{3}}{2}\hat{y}\right) \\ \mathbf{b}_2 &= \frac{4\pi}{3a}\left(\frac{1}{2}\hat{x} - \frac{\sqrt{3}}{2}\hat{y}\right). \end{aligned} \tag{2.2}$$

With the lattice structure suitably defined for graphene in both real space and reciprocal space, we now turn our attention to the tight-binding Hamiltonian for graphene. In graphene, to very good approximation, the states are spin degenerate [3, 20–25]. Thus, ignoring spin, the tight-binding Hamiltonian for graphene with only nearest-neighbor hopping is given by:

$$H = \gamma_0 \sum_{\langle ij \rangle} c^\dagger_{A,i} c_{B,j} + \text{h.c.} \tag{2.3}$$

where $c^\dagger_{\alpha,i}$ ($c_{\alpha,i}$) creates (annihilates) an electronic state at site i on sublattice α, $\langle ij \rangle$

denotes a sum over nearest-neighbors, and γ_0 is the nearest-neighbor hopping. We choose to write γ_0 to be consistent with the naming convention of the Slonczewski-Weiss-McClure model of graphite whose conventions we will also employ in our study of bilayer graphene.

We make the transformation to crystal momentum space by writing

$$c_{\alpha,i} = \frac{1}{\sqrt{N}} \sum_{\mathbf{k}} e^{-i\mathbf{k}\cdot(\mathbf{r}_i + \mathbf{d}_\alpha)} c_{\alpha,\mathbf{k}}$$

where the sum extends over the first Brillouin zone, N is the number of lattice sites, $\mathbf{r}_i$ is the real space vector associated with site i, and α is the sublattice label. After this transformation, it is straightforward to show that H becomes $H = \sum_{\mathbf{k}} \Psi_{\mathbf{k}}^\dagger \hat{h}_{\mathbf{k}} \Psi_{\mathbf{k}}$ where $\Psi_{\mathbf{k}} = (c_{A,\mathbf{k}}\ c_{B,\mathbf{k}})^{\mathrm{T}}$ and $\hat{h}_{\mathbf{k}}$ is the Hamiltonian matrix which we can write in sublattice space as:

$$\hat{h}_{\mathbf{k}} = \begin{pmatrix} 0 & \gamma_0 S(\mathbf{k}) \\ \gamma_0 S(\mathbf{k})^* & 0 \end{pmatrix} \tag{2.4}$$

where $S(\mathbf{k}) = e^{-iak_x} + 2e^{i\frac{a}{2}k_x} \cos\frac{a\sqrt{3}}{2}k_y$ comes from the sum over the nearest neighbors during the transformation to k-space. It is instructive to look at the resulting band structure given by $E_\pm(\mathbf{k}) = \pm\gamma_0\sqrt{3 + 2\cos a\sqrt{3}k_y + 4\cos\frac{a\sqrt{3}}{2}k_y \cos\frac{3a}{2}k_x}$ and shown in Fig. 2.3. From Fig. 2.3 we see that at certain points in the Brillouin zone the dispersion vanishes, these correspond to the points K and K' as shown in Fig. 2.2. From Fig. 2.3 we can see that around these points of vanishing energy the dispersion appears linear in momentum, reminiscent of massless relativistic particles. These regions are referred to as the K and K' valleys. By expanding Eq. 2.4 around these points we will see that the effective Hamiltonian in these valleys appears to be a two-dimensional analogue of the Dirac equation for massless relativistic particles.

To examine the effective Hamiltonian at the Brillouin zone corners K and K' we perform a Taylor series expansion of $S(K + \mathbf{p})$ and $S(K' + \mathbf{p})$ around $\mathbf{p} = 0$. After

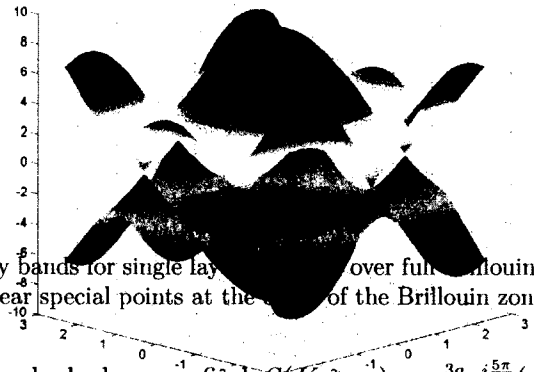

FIG. 2.3: Energy bands for single lay[illegible] over full [illegible]louin zone. Notice the dispersion appears linear near special points at the [illegible] of the Brillouin zone.

some straightforward algebra we find $S(K + \mathbf{p}) \approx \frac{3a}{2}e^{i\frac{5\pi}{6}}(p_x - ip_y)$ and $S(K' + \mathbf{p}) \approx \frac{3a}{2}e^{i\frac{5\pi}{6}}(p_x + ip_y)$. We can absorb the phase $e^{i\frac{5\pi}{6}}$ into the definition of $\mathbf{\Psi_k}$ by performing a unitary transformation in each valley. Thus, around the K and K' points the Hamiltonian matrix can be written as:

$$\begin{aligned} \hat{h}^K_{\mathbf{k}} &= \begin{pmatrix} 0 & \hbar v_F(k_x - ik_y) \\ \hbar v_F(k_x + ik_y) & 0 \end{pmatrix} \\ \hat{h}^{K'}_{\mathbf{k}} &= \begin{pmatrix} 0 & \hbar v_F(k_x + ik_y) \\ \hbar v_F(k_x - ik_y) & 0 \end{pmatrix} \end{aligned} \tag{2.5}$$

where $v_f = \frac{3a\gamma_0}{2\hbar}$. We can make the analogy to the Dirac equation more explicit by rewriting these matrices in terms of Pauli matrices $\hat{h}^K_{\mathbf{k}} = \hbar v_F \boldsymbol{\sigma} \cdot \mathbf{k}$ and $\hat{h}^{K'}_{\mathbf{k}} = \hbar v_F \boldsymbol{\sigma}^* \cdot \mathbf{k}$. Then, following the prescription $p_i \rightarrow -i\frac{\partial}{\partial x_i}$ we obtain $\hat{h}^K_{\mathbf{x}} = -i\hbar v_F \boldsymbol{\sigma} \cdot \nabla_{\mathbf{x}}$ and $\hat{h}^{K'}_{\mathbf{x}} = -i\hbar v_F \boldsymbol{\sigma}^* \cdot \nabla_{\mathbf{x}}$, which are two-dimensional analogues of the Dirac equation for massless particles [8].

Notice that the eigenstates of Eq. 2.5, in addition to being eigenstates of energy are also eigenstates of the operator $\mathbf{k} \cdot \boldsymbol{\sigma}/k$ which, if σ_i were a spin operator, would be a helicity operator. However, retracing our derivation we see that σ_i exists in sublattice space. Therefore, by identifying the sublattice degree of freedom as a sublattice pseudospin we see that the direction of the pseudospin in graphene is locked with the direction of the crystal momentum. In this sense the electronic states in graphene are chiral. The chiral nature of these states leads to the suppression of backscattering of electronic states in graphene and affects many of its electronic properties including quantum Hall effect and localization [2, 3, 7, 8].

It turns out that the gapless nature of these states is a symmetry-protected property of graphene related to the system's invariance under time-reversal and spatial inversion. Under time reversal, $\mathcal{T}$, the Hamiltonian at the K point transforms as $\mathcal{T} : \hat{h}_K \rightarrow \hat{h}^*_{K'}$, while under spatial inversion, $\mathcal{I}$, sublattice A and B are exchanged and so we have $\mathcal{I} : \hat{h}_K \rightarrow \sigma_1 \hat{h}_{K'} \sigma_1$. Thus, under simultaneous time reversal and spatial inversion we have $\mathcal{TI} : \hat{h}_K \rightarrow \sigma_1 \hat{h}^*_K \sigma_1$. In pristine graphene the symmetry of the crystal combined with the equivalence of the A and B sublattices impose spatial inversion symmetry while the absence of a magnetic field imposes time-reversal symmetry. Ergo, at the K (and, equivalently, K') point we have the restriction that:

$$\hat{h}_K = \sigma_1 \hat{h}^*_K \sigma_1.$$

Now, because $\hat{h}_K$ is a 2×2 hermitian matrix it can be expressed as the sum of Pauli matrices:

$$\hat{h}_K = \sum_{i=1}^{3} h_i \sigma_i.$$

By imposing the above constraint due to symmetry we can see that $h_3 = 0$ which means

that the system cannot develop a gap at the K or K' point without breaking either time-reversal or spatial inversion symmetry. This proof suggests that one could potentially open a band gap by breaking the sublattice symmetry, as has been investigated both theoretically [26] and experimentally using hexagonal boron nitride as a substrate [27].

2.1.2 Bilayer Graphene: A Novel Chiral Hamiltonian

When graphene is made through micromechanical cleavage, frequently the resulting samples contain regions of bilayer graphene [9–11]. The most common stacking arrangement for bilayer graphene in nature is the A-B stacking, also known as Bernal stacking, shown in Fig. 2.4. In this arrangement atoms from sublattice A of the top layer sit on top of atoms from sublattice B of the bottom layer. To model the behavior of electrons

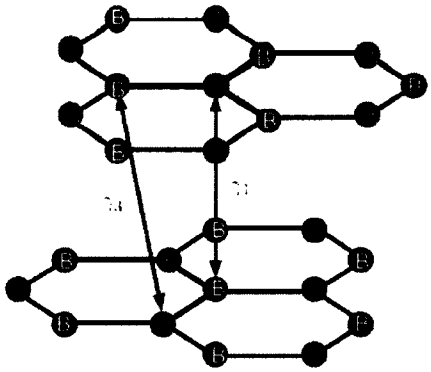

FIG. 2.4: Bernal stacked bilayer graphene lattice with hopping parameters γ_1, and γ_3 labeled.

in these systems one can employ a tight-binding model similar to the case of single layer graphene but, in addition to the intralayer hopping parameter γ_0, we must include the various relevant interlayer hopping parameters, the most important of which are labeled

in Fig. 2.4 [8, 11, 28, 28, 29]. This tight-binding Hamiltonian can be written:

$$H = \gamma_0 \sum_{\langle ij \rangle} \sum_m \left(c^\dagger_{A,m,i} c_{B,m,j} + \text{h.c.} \right) + \gamma_1 \sum_i \sum_m \left(c^\dagger_{A,1,i} c_{B,2,i} + \text{h.c.} \right) + \gamma_3 \sum_{\langle ij \rangle} \left(c^\dagger_{A,2,i} c_{B,1,j} + \text{h.c.} \right) + \frac{\Delta}{2} \sum_{i,m,\alpha} (-1)^{2m} \left(c^\dagger_{\alpha,m,i} c_{\alpha,m,i} + \text{h.c.} \right) \tag{2.6}$$

where $c^\dagger_{\alpha,m,i}$ ($c_{\alpha,m,i}$) creates (annihilates) an electronic state on sublattice α in layer m at site i, γ_0 is the same intralayer hopping term inherited from single layer graphene, γ_1 is the direct hopping parameter from sublattice A in layer 1 to sublattice B directly beneath in layer 2, γ_3 is the hopping term coupling states in sublattice B of layer 1 with the three nearest neighbor sites on sublattice A of layer 2, and Δ takes into account a possible electric bias between the two layers. Other hopping terms can also be included in Eq. 2.6 however these are much smaller than γ_0, γ_1 and γ_3 and have been shown to have a minimal effect on the low energy electronic properties [8, 11, 28, 28, 29]. Following a similar analysis to the previous section we can find the Hamiltonian matrix for bilayer graphene in k-space. Once again we find there are two decoupled valleys, K and K'. In the K valley, the effective Hamiltonian for bilayer graphene takes the form $H = \sum_{\mathbf{k}} \Psi^\dagger_{\mathbf{k}} \hat{h}^{\text{BLG}}_{\mathbf{k}} \Psi_{\mathbf{k}}$ where $\Psi_{\mathbf{k}} = (c_{A,1,\mathbf{k}}\ c_{B,1,\mathbf{k}}\ c_{A,2,\mathbf{k}}\ c_{B,2,\mathbf{k}})^{\text{T}}$ and the Hamiltonian matrix for bilayer graphene is:

$$\hat{h}^{\text{BLG}}_{\mathbf{k}} = \begin{pmatrix} \Delta/2 & \hbar v_F (k_x - i k_y) & 0 & 3\gamma_3 a (k_x + i k_y) \\ \hbar v_F (k_x + i k_y) & \Delta/2 & \gamma_1 & 0 \\ 0 & \gamma_1 & -\Delta/2 & \hbar v_F (k_x - i k_y) \\ 3\gamma_3 a (k_x - i k_y) & 0 & \hbar v_F (k_x + i k_y) & -\Delta/2 \end{pmatrix}. \tag{2.7}$$

This can be rewritten in a more compact notation:

$$\begin{aligned}\hat{h}_{\mathbf{k}}^{\mathrm{BLG}} = &\frac{\Delta}{2}\tau_3 + \hbar v_F(k_x\sigma_1 + k_y\sigma_2) + \frac{\gamma_1}{2}(\sigma_1\tau_1 + \sigma_2\tau_2) \\ &+ \frac{3}{2}\gamma_3 a\left[k_x(\sigma_1\tau_1 - \sigma_2\tau_2) - k_y(\sigma_1\tau_2 + \sigma_2\tau_1)\right]\end{aligned} \tag{2.8}$$

where σ_i and τ_i are Pauli matrices acting in sublattice space and layer space, respectively. As shown in Fig. 2.5 this model has four bands with roughly parabolic dispersion at low energy, interpolating to a more linear dispersion at higher energy. One pair of bands is separated by a gap equal to γ_1 due to the formation of interlayer dimer states [28]. At very small wavevectors the term proportional to γ_3 breaks up this parabolic dispersion into four linear dispersions separated in k-space, Fig. 2.5, and thus adds a trigonal warping to the otherwise isotropic bands. This property of the γ_3 term can manifest itself as qualitative features in the linear response of this system, as we show in Chapter 3.

Notice that, in the absence of an interlayer bias ($\Delta = 0$), just as in the case of single layer graphene, this Hamiltonian admits gapless zero energy states due to the preservation of inversion symmetry. However, by applying an electric field perpendicular to the plane of the crystal an interlayer bias can be generated ($\Delta \neq 0$) which breaks the inversion symmetry and consequently opens a gap as shown in Fig. 2.5(b). By varying the strength of the electric field this gap can be tuned, as shown experimentally [12–17], and can manifest itself in the screening and collective properties of the systems as we explore in Chapter 3.

Notice that, unlike the case with single layer graphene, this Hamiltonian is not manifestly chiral due to the additional hopping terms. However, as shown in [28] at low energies, $E << \gamma_1$, the split dimer bands can be neglected and this four band model Hamiltonian can

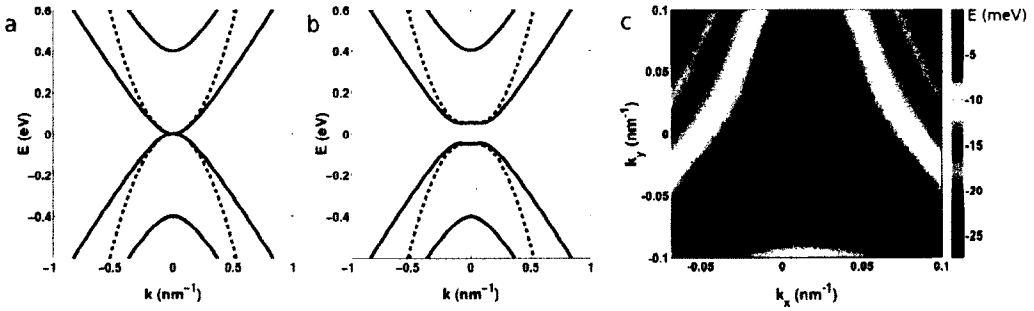

FIG. 2.5: Energy bands for bilayer graphene. (a) Bilayer graphene dispersion calculated without trigonal warping and without a bias, $\Delta = 0$, using the four-band model (solid) and two-band model (dashed). (b) same as (a) but with $\Delta = 100$meV. (c) Plot of dispersion near zero energy showing the effect of trigonal warping.

be projected onto the low energy bands to arrive at the following two-band Hamiltonian:

$$\hat{h}_{\mathbf{k}}^{\mathrm{BLG}} = \begin{pmatrix} \Delta/2 & \frac{\hbar^2}{2m}(k_x - ik_y)^2 \\ \frac{\hbar^2}{2m}(k_x + ik_y)^2 & -\Delta/2 \end{pmatrix}. \tag{2.9}$$

Unlike the four-band model in Eq. 2.7, in the absence of a an interlayer bias, the bands for this model are exactly parabolic, Fig. 2.5, with effective mass $m = \gamma_1/2v_F^2$. Furthermore, we can express this Hamiltonian in terms of Pauli matrices as:

$$\hat{h}_{\mathbf{k}}^{\mathrm{BLG}} = \frac{\hbar^2}{2m}(\boldsymbol{\sigma} \cdot \mathbf{k})^2 + \frac{\Delta}{2}\sigma_3. \tag{2.10}$$

For $\Delta = 0$, we can see that the eigenstates of this two-band Hamiltonian are manifestly chiral, but not in the same way as single layer graphene. Instead of winding once around the unit sphere in momentum space, the pseudospin vector for states in bilayer graphene winds twice around the unit sphere, as shown in Fig. 2.1(b). This novel chirality allows backscattering, unlike single layer graphene, but has a number of unique signatures in both quantum Hall experiments [28] and screening which we will discuss in Chapter 3.

2.2 Topological Insulators

Another example of a two-dimensional condensed matter system hosting Dirac-like Fermions is the surface of a three-dimensional topological insulator or, more precisely, the interface between a trivial insulator, like the vacuum, and a strong three-dimensional topological insulator (3DTI), like Bi_2Se_3 [30, 31]. At such an interface surface states may be labeled with a two-dimensional crystal momentum $\mathbf{k}$ and the behavior of the symmetry-protected Dirac states can be described by the Hamiltonian matrix [30–33]:

$$H_{\mathbf{k}} = \hbar v_F \hat{n} \cdot (\boldsymbol{\sigma} \times \mathbf{k}) \tag{2.11}$$

where v_F is the velocity associated with the linearly dispersing surface states, $\hat{n}$ is the unit vector normal to the interface, and $\boldsymbol{\sigma}$ is the vector of Pauli matrices in spin space. A number of real materials have been confirmed to fall into this class, including: the alloy $Bi_{1-x}Sb_x$, and the stoichiometric crystals Bi_2Se_3, Bi_2Te_3, and Sb_2Te_3. In this section we will provide some background on three-dimensional topological insulators, explain the reason they are protected by symmetry and elucidate the sense in which these insulators are "topological".

According to the band theory of solids, electronic states in a crystal are characterized by a crystal momentum, $\mathbf{k}$, defined in a periodic Brillouin zone. The Bloch states, $|u_m(\mathbf{k})\rangle$, are defined in a single unit cell and are eigenstates the Bloch Hamiltonian, $H(\mathbf{k})$, with eigenvalues, $E_m(\mathbf{k})$, defining a band structure in k-space. Within this paradigm, a material is an insulator when there is a gap between the filled valence bands and the empty conduction bands. While the size of the band gaps may differ between insulators one can imagine tuning the parameters of $H(\mathbf{k})$ to interpolate continuously between them without closing the energy gap. In this sense one can define equivalence classes for insulators. The

vacuum from relativistic quantum mechanics can be viewed as possessing a gap formed between a filled valence band of positrons and a conduction band of electrons and is thus an insulator. We will define a trivial insulator as one that is in the same equivalence class as the vacuum. Topological insulators are those insulators which are not equivalent to the vacuum. As we will explain, it is possible to assign a topological invariant to describe the equivalence classes of different insulators.

One state with a gapped spectrum not equivalent to the vacuum is an integer quantum Hall state. This state arises when electrons are confined to two-dimensions and subjected to a strong magnetic field leading to quantized circular orbits and a quantized spectrum of Landau levels with energies $E_n = \hbar\omega_c(n + 1/2)$ where ω_c is the cyclotron frequency. If an integer number, N, of Landau levels are filled then it is clear that an energy gap exists between the occupied and empty levels, just like in an insulating state. However, unlike a trivial insulator, the application of an electric field will cause the cyclotron orbits to drift generating a Hall current described by the quantized Hall conductivity

$$\sigma_{xy} = \frac{Ne^2}{h}.$$

It was shown in [34], by computing σ_{xy} using the Kubo formula, that the integer, N, quantizing the Hall conductivity is identical to the total Chern number $n = \sum_m n_m$ where the sum is over the occupied bands and n_m is the Chern number associated with band m defined by

$$n_m = \frac{i}{2\pi} \int d\mathbf{k} \nabla \times \langle u_m(\mathbf{k}) | \nabla_{\mathbf{k}} | u_m(\mathbf{k}) \rangle \tag{2.12}$$

where the integral is taken over the Brillouin zone. The Chern number is invariant in the sense that smooth variations in the Hamiltonian cannot change it. Therefore, it can be used to define equivalence classes of 2D insulators distinguished by different values of

$n \in \mathbb{Z}$. However, the Hall conductivity is odd under time reversal, $\mathcal{T}$, [30, 35] so this formalism doesn't apply in a $\mathcal{T}$-invariant system.

Before we continue our discussion of topological insulators, it will help us to establish a result known as Kramer's theorem which states that if a spin 1/2 particle is described by a $\mathcal{T}$-invariant Hamiltonian H then all eigenstates of H are degenerate. To prove this we start by noting that the time reversal operator may be represented as $T = e^{i\pi S_y/\hbar}K$ where S_y is the spin operator and K is the complex conjugation operator. Then we assume that, on the contrary, there exists an eigenstate, $|\psi\rangle$, of H which is not degenerate. Since T commutes with H we know that $|\psi\rangle$ is also an eigenstate of T with non-zero eigenvalue c. Thus:

$$T|\psi\rangle = c|\psi\rangle$$
$$T^2|\psi\rangle = |c|^2|\psi\rangle.$$

Furthermore, it is straightforward to show that for a spin 1/2 system $T^2|\psi\rangle = -|\psi\rangle$ and hence $|c|^2 = -1$. Therefore, we have arrived at a contradiction and must conclude that all eigenstates of H are degenerate. In a system with no spin-orbit coupling this degeneracy is the usual spin degeneracy; however, in systems in which spin-orbit coupling splits this degeneracy Kramer's theorem has nontrivial implications.

If a Bloch Hamiltonian, $H(\mathbf{k})$, is $\mathcal{T}$-invariant then under time reversal we have

$$TH(\mathbf{k})T^{-1} = H(-\mathbf{k}).$$

It turns out that the Chern number as defined above vanishes in these systems. However, it is possible to define equivalence classes of topologically distinct 2D $\mathcal{T}$-invariant insulators

characterized by a $\mathbb{Z}_2$ index, $\nu = 0, 1$. One way to see that this index should be in $\mathbb{Z}_2$ is to consider the boundary of the 2D $\mathcal{T}$-invariant insulator with strong spin-orbit coupling. If there are edge states at the boundary, by Kramer's theorem the bands must be degenerate at special $\mathcal{T}$-invariant points in the 1D projected Brillouin zone: $k = 0$ and π/a. Away from these points the spin-orbit coupling will split the degeneracy. However, between these two points the bands must cross the Fermi surface either an even or an odd number of times. If the bands cross the Fermi surface an even number of times then the edge state bands can be smoothly pushed either below or above the Fermi surface and thus be removed without closing the gap. However, if the edge state bands cross the Fermi surface an odd number of times they cannot be smoothly pushed out of the gap without closing it. Whether or not there are edge states and how many times they cross the Fermi surface is determined by the topological class of the 2D bulk Hamiltonian.

The $\mathbb{Z}_2$ index characterizing the topological classes of 2D $\mathcal{T}$-invariant insulators may be formulated in terms of the unitary matrix:

$$w_{mn}(\mathbf{k}) = \langle u_m(\mathbf{k})|T|u_n(-\mathbf{k})\rangle$$

where T is the time-reversal operator and $|u_n(\mathbf{k})\rangle$ is an occupied Bloch state. In the 2D Brillouin zone there are four points, Γ_a, where $|u_n(\Gamma_a)\rangle = |u_n(-\Gamma_a)\rangle$. It can be shown that $w_{mn}(\Gamma_a)$ is an antisymmetric matrix and so its determinant is the square of its Pfaffian. Thus, we can see that

$$\delta_a \equiv \frac{\mathrm{Pf}[w(\Gamma_a)]}{\sqrt{\det[w(\Gamma_a)]}} = \pm 1.$$

With this definition it can be shown that the $\mathbb{Z}_2$ invariant, ν, is given by

$$(-1)^\nu = \prod_{a=1}^{4} \delta_a. \tag{2.13}$$

This formulation can be generalized to three-dimensional (3D) $\mathcal{T}$-invariant insulators. However, in 3D we define four $\mathbb{Z}_2$ topological indices $(\nu_0; \nu_1, \nu_2, \nu_3)$. These indices are related to the Pfaffian of the T operator evaluated at the eight T-invariant points of the bulk 3D Brillouin zone. Thus, there exist 16 distinct classes of 3DTIs however, the index ν_0 determines two main categories of 3DTIs: the weak topological insulators (WTI) for $\nu_0 = 0$, and strong topological insulators (STI) for $\nu_0 = 1$ [5]. The WTIs possess an even number of Dirac points in the surface 2D Brillouin zone, while the STIs possess an odd number of Dirac points. While the WTI surface states are vulnerable to localization via disorder the STI surface states cannot be localized even in the presence of strong disorder [5, 30]. For a STI, by $\mathcal{T}$-symmetry, states with opposite momentum possess opposite spins leading to a Berry phase of π. This in fact leads to weak antilocalization [30].

Bi_2Se_3 is an example of a STI with one Dirac cone located at the center of the 2D Brillouin zone, whose states are described by Eq. 2.11. This appears to violate the Nielsen-Ninomiya Fermion doubling theorem [36] which states that it is impossible to construct a non-interacting lattice hopping model possessing an odd number of chiral Fermion states [3]. However, the Nielsen-Ninomiya theorem is circumvented in this case because it can be shown that the interface on the opposite side of the bulk possesses the Dirac states with opposite chirality [3, 30].

Due to their unique spin chirality, research on topological insulators has exploded in recent years. After the alloy $Bi_{1-x}Sb_x$ was found to host chiral Dirac surface states, using spin polarized ARPES [37], the stoichiometric crystals of Bi_2Se_3, Bi_2Te_3, and Sb_2Te_3 were found to host similar states. The fact that these are stoichiometric crystals means they are easier to grow and control. Furthermore, their surface states are nearly perfect Dirac cones and, unlike $Bi_{1-x}Sb_x$, they possess sizable bulk band gaps. For instance, Bi_2Se_3 has a bulk band gap of 0.3eV meaning the topological surface states persist to room temperature [30]. In Chapter 4 we study the possibility of inducing the same spin chirality associated with

3DTI surface states in graphene via proximity effect. While in Chapter 5 we study some of the possible exotic superconducting states that can be induced at the interface between a 3DTI and a superconductor. Finally, in Chapter 6 we explore the effect of interactions on these surface states.

CHAPTER 3

Screening and Collective Modes in Gapped Bilayer Graphene

This chapter is based on the work found in [38]. As we touched on in Chapter 2, bilayer graphene (BLG) has many unique electronic properties that make it an extremely interesting system. In this chapter we focus on BLG that is formed by two Bernal stacked layers of graphene. When placed on an insulating substrate the electrons in BLG form an ideal two-dimensional electron gas (2DEG) with a very high room temperature mobility, in particular when Boron Nitride is used as a substrate [39–41]. In pristine BLG the conduction and valence bands touch at points, charge neutrality points (CNPs), at the corners of the Brillouin zone. At very low energy around these points the bands are approximately parabolic. However, by applying a perpendicular electric field inversion symmetry can be broken opening a band-gap (Δ) proportional to the interlayer bias [12–17]. Moreover, recent experiments [42–45] provide strong evidence that at low temperatures and dopings the electrons in BLG might be in a spontaneously broken symmetry state [46–55]. All these facts make BLG an extremely interesting system both from a fundamental physics

point of view and for its possible technological applications. As a consequence the accurate knowledge of the electronic properties of BLG is of great interest.

One of the most important physical quantities to characterize the electronic properties of a system is the dielectric function $\epsilon(\mathbf{q}, \omega)$. This quantity determines the effective, screened, Coulomb interaction among the electrons in the system and is therefore essential for the calculation of all the electronic properties. Experiments suggest that in most BLG samples charge impurities close to the surface of the substrate or placed between the substrate and the BLG layer are the dominant source of scattering [11]. In this situation knowledge of the static dielectric function, $\epsilon(\mathbf{q}, \omega = 0)$ is essential to calculate the d.c. conductivity. Moreover, in the case of magnetic adatoms placed on BLG, the static polarizability determines the effective Ruderman-Kittel-Kasuya-Yoshida (RKKY) interaction between the magnetic adatoms [1]. The dynamic dielectric function determines the optical properties of the system and the collective electronic modes, plasmons. Previous works [56–61] have studied the case of gapless BLG (in addition to gapless single and multilayer systems [62–64]). In the presence of a gap some of the symmetries that simplify the calculation of the response functions in gapless BLG disappear. In part for this reason the only results available [65] for the dielectric function in gapped BLG were obtained using the simplified effective low energy 2-band model discussed in Chapter 2 [28, 29]. This model neglects features of the band-structure of BLG that can strongly affect the response function, especially when $\Delta \neq 0$. In particular, in the 4-band model, in the presence of a band-gap the bands, at low energy, acquire a characteristic "sombrero" shape [28], see Fig. 3.1 (a), that is not captured by the simplified 2-band model. In this work we obtain $\epsilon(\mathbf{q}, \omega)$ for gapped graphene using the full 4-band model and the random phase approximation (RPA). We find that the nonmonotonic dispersion of the fermionic excitations close to the CNP profoundly modifies the static and dynamic screening properties of BLG. In addition we study the effect of trigonal warping on $\epsilon(\mathbf{q}, \omega)$. In all calculations in this chapter we

assume translation invariance.

3.1 Model

As discussed in Chapter 2, the four-band continuum model Hamiltonian for BLG can be expressed as $H_0 = \sum_{\mathbf{k}} \Psi^\dagger_{\mathbf{k}} h(\mathbf{k}) \Psi_{\mathbf{k}}$ where $\Psi^\dagger_{\mathbf{k}}$ ($\Psi_{\mathbf{k}}$) is the 4-component creation (annihilation) operator $\Psi^\dagger_{\mathbf{k}} = (a^\dagger_{\mathbf{k},1}, b^\dagger_{\mathbf{k},1}, a^\dagger_{\mathbf{k},2}, b^\dagger_{\mathbf{k},2})$ ($\Psi_{\mathbf{k}} = (a_{\mathbf{k},1}, b_{\mathbf{k},1}, a_{\mathbf{k},2}, b_{\mathbf{k},2})$) with $a^\dagger_{\mathbf{k},i}$ ($a_{\mathbf{k},i}$), $b^\dagger_{\mathbf{k},i}$ ($b_{\mathbf{k},i}$) the creation (annihilation) operator for an electron with wavevector $\mathbf{k}$ in layer i on sublattice A and B respectively, and $h(k)$ is the matrix

$$h(\mathbf{k}) = \frac{\Delta}{2}\tau_z + \hbar v_F(k_x\sigma_x + k_y\sigma_y) - \frac{\gamma_1}{2}(\sigma_x\tau_x + \sigma_y\tau_y) + \frac{3}{2}\gamma_3 a\left[k_x(\sigma_x\tau_x - \sigma_y\tau_y) - k_y(\sigma_x\tau_y + \sigma_y\tau_x)\right]. \tag{3.1}$$

In Eq.3.1 σ's, τ's are 2x2 Pauli matrices representing the sublattice and layer degrees freedom respectively, v_F is the Fermi velocity at the Dirac point of a single graphene layer, γ_1 is the direct hopping parameter (from a site on sublattice A in layer 1 to the nearest neighbor site on sublattice B in layer 2), γ_3 is the trigonal warping hopping parameter (from a site on sublattice B in layer 1 to the three nearest neighbors on sublattice A in layer 2), $a = 1.42\text{Å}$ is the in-plane lattice constant, and Δ is the band gap at $k = 0$. Throughout this work, for concreteness, we assume $v_F = 10^6\text{m/s}$, $\gamma_1 = 0.35\text{eV}$, and $\gamma_3 = (3/4)\gamma_1 = 0.26\text{eV}$, however the main features of our results do not depend on the precise values chosen for these parameters.

The Coulomb interactions are described by the Hamiltonian

$$H_i = (1/2A)\sum_{\mathbf{q}}[V_+(q)\hat{\rho}_{\mathbf{q}}\hat{\rho}_{-\mathbf{q}} + V_-(q)\hat{d}_{\mathbf{q}}\hat{d}_{-\mathbf{q}}]$$

where A is the sample area, $\hat{\rho}_{\mathbf{q}}$ ($\hat{d}_{\mathbf{q}}$) the operator for the sum (difference) of the densities $\hat{\rho}_{\mathbf{q},i}$ in the two layers, $V_{\pm}(q) = (V_S(q) \pm V_D(q))/2$ with $V_S(q) = 2\pi e^2/(\epsilon q)$ the Coulomb interaction between electrons in the same layer and $V_D = 2\pi e^2(e^{-qd})/(\epsilon q)$ the Coulomb interaction between electrons in different layers, $d = 3.35$Å the distance between the two layers, and ϵ the background dielectric constant. For the work presented in this chapter we assume $\alpha \equiv e^2/\epsilon\hbar v_F = 0.5$ and temperature $T = 0$.

3.2 Polarizability and Dielectric Function

For most of the electronic quantities of interest, such as the conductivity, as long as $q \ll 1/d$ BLG can be treated as a single 2D electronic system and therefore the dielectric function that enters the calculation of these quantities is the one associated with the sum of the densities in the two layers. Within the random phase approximation we may express this dielectric function as:

$$\epsilon(\mathbf{q},\omega) = 1 - V_+(\mathbf{q})\Pi(\mathbf{q},\omega)$$

where

$$\Pi(\mathbf{q},\omega) = g\sum_{\lambda,\lambda'}\int \frac{d\mathbf{k}}{(2\pi)^2}\frac{n_{\lambda,\mathbf{k}} - n_{\lambda',\mathbf{k}+\mathbf{q}}}{\hbar\omega + \epsilon_{\lambda,\mathbf{k}} - \epsilon_{\lambda',\mathbf{k}+\mathbf{q}} + i\eta} \times |(U_{\mathbf{k}}^{\dagger}U_{\mathbf{k}+\mathbf{q}})_{\lambda,\lambda'}|^2 \tag{3.2}$$

is the polarizability, also known as the density-density response function. The polarizability describes the response of the electron density to an external field that couples to the density operator as explained in [1]. In Eq. 3.2 $g = g_s g_v = 4$ is the total spin (g_s) and valley (g_v) degeneracy, λ, λ' are the band indices, $n_{\lambda,\mathbf{k}}$ is the Fermi-Dirac distribution function for a particle in band λ with wavevector $\mathbf{k}$, $\epsilon_{\lambda,\mathbf{k}}$ is the energy of a fermionic state in band λ with

momentum $\mathbf{k}$, and $U_{\mathbf{k}}$ is the unitary matrix that diagonalizes the Hamiltonian H_0. From Fig. 3.1 (b) we see that the intraband wave-function overlap $|(U_{\mathbf{k}}^{\dagger}U_{\mathbf{k+q}})_{\lambda,\lambda}|^2$ for the 4-band model is quite different from the one for the 2-band model, especially when $\Delta \neq 0$.

In Fig. 3.1 (c) the results for the static polarizability $\Pi(\mathbf{q}, \omega = 0)$ are shown for fixed doping $n = 10^{12}$ cm^{-2} and different values of Δ. We see that for $\Delta \neq 0$ the results obtained with the 4-band model are quite different from the ones obtained with the 2-band model. In the 2-band model $\Pi(\mathbf{q}, 0)$ exhibits a cusp, associated with a Kohn anomaly, only for $q = 2k_F$ (k_F being the Fermi wavevector), whereas in the 4-band model $\Pi(\mathbf{q}, 0)$ exhibits Kohn anomalies also for values of $q < 2k_F$. This is due to the non-monotonic behavior exhibited by the low energy band structure in the 4-band model for $\Delta \neq 0$, Fig. 3.1 (a). Consequently, in the 4-band model, for $\Delta \neq 0$, for fixed n (Δ) when $\Delta > \Delta_c \equiv \hbar v_F \sqrt{\pi n}$ ($|n| < n_c \equiv \Delta^2/(\pi \hbar^2 v_F^2)$) the Fermi surface is multiply connected. Neglecting trigonal warping for $n < n_c$ the Fermi surface is formed by two circumferences, of radius $k_{F\pm} = (1/\hbar v_F)\sqrt{\epsilon_F^2 + \Delta^2/4 \pm \sqrt{\epsilon_F^2(\gamma_1^2 + \Delta^2) - \Delta^2/4}}$ respectively, with $\epsilon_F = (1/2)\sqrt{(\hbar^4 v_F^4 \pi^2 n^2 + \Delta^2\gamma_1^2)/(\gamma_1^2 + \Delta^2)}$ (see inset of Fig. 3.1 (b)). In this situation we can expect additional Kohn anomalies corresponding to values of q joining points on the same connected part of the Fermi surface and on disconnected parts of the Fermi surface. For $n = 10^{12}$ cm^{-2} we have that $\Delta_c \approx \gamma_1/3$. When $\Delta = \Delta_c$ the Fermi energy just touches the top of the sombrero. In this case we only have one additional Kohn anomaly for $q = k_F$ in addition to the $q = 2k_F$ one, see Fig. 3.1 (c). For $\Delta > \Delta_c$ the Fermi energy cuts the sombrero region and so we have Kohn anomalies for $q = k_{F+} - k_{F-}$, and $q = 2k_{F-}$ in addition to the one for $q = 2k_{F+}$ as shown in Fig. 3.1 (c). Intuitively, one might expect to observe an additional anomaly for $q = k_{F+} + k_{F-}$, however the points on the Fermi surface connected by this value of q have Fermi velocities with the same sign and therefore the anomaly is suppressed. Fig. 3.1 (d) shows the dependence of $\Pi(\mathbf{q}, 0)$ on q and the density for $\Delta = \gamma_1/2$. From this figure we see the evolution of the Kohn anomalies with doping

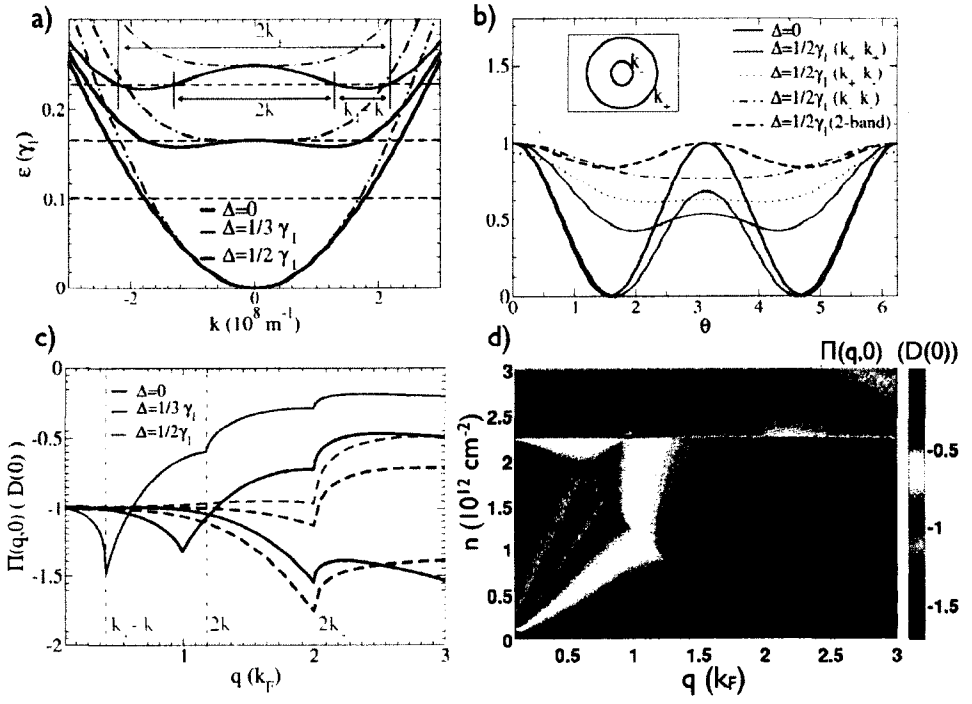

FIG. 3.1: Static polarizability, band structure, and chirality factors for bilayer graphene. (a) Lowest conduction band for $\Delta = \gamma_1/2,\ \gamma_1/3,\ 0$. The solid (dash-dot) curves are obtained using the 4-band (2-band) model. The horizontal dashed lines indicate the 4-band Fermi energy for doping $n = 10^{12}\text{cm}^{-2}$ for $\Delta = \gamma_1/2,\ \gamma_1/3,\ 0$ from top to bottom. (b) Chirality factors, $|(U_{\mathbf{k}}^{\dagger}U_{\mathbf{k}'})_{\lambda\lambda}|^2$, evaluated for $|\mathbf{k}| = |\mathbf{k}'| = k_F$ for the 2-band model at $\Delta = 0,\ \gamma_1/2$, denoted by the black solid and dashed lines respectively, and the 4-band model for $\Delta = \gamma_1/2,\ 0$. θ is the angle between $\mathbf{k}$ and $\mathbf{k}'$. For the case $\Delta = \gamma_1/2$ in the 4-band model there are three possible intraband overlap scenarios we can consider: (i) $\mathbf{k}$ and $\mathbf{k}'$ both lie on the Fermi surface at wavevector k_{F+}, (ii) $\mathbf{k}$ and $\mathbf{k}'$ both lie on the Fermi surface at wavevector k_{F-}, (iii) $\mathbf{k}$ lies on the Fermi surface at wavevector k_{F+} while $\mathbf{k}'$ lies on the fermi surface at k_{F-}. (c) $\Pi(\mathbf{q}, 0)$ for $n = 10^{12}\text{cm}^{-2}$ without trigonal warping. Solid (dashed) curves are the results obtained using the 4-band (2-band) model. (d) Contour plot of polarizability, $\Pi(q, n, \omega = 0)$, as a function of q and doping n for $\Delta = 1/2\gamma_1$.

in gapped BLG, in particular we can observe the merging of some of the anomalies for specific values of the doping.

As discussed in Chapter 2 and displayed in the left panels of Fig. 3.2, in the presence of trigonal warping the energy-bands become anisotropic [28, 29]. In particular, at low energies the lowest bands exhibit four degenerate minima. The modifications of the fermionic energy bands due to the trigonal warping are reflected in the polarizability, as shown by the right panels of Fig. 3.2. $\Pi(\mathbf{q}, 0)$ becomes strongly anisotropic, the number and position of the Kohn anomalies becomes dependent on the direction of $\mathbf{q}$.

The dynamic dielectric function $\epsilon(\mathbf{q}, \omega)$ for fixed doping $n = 10^{12}$ cm^{-2} and $\Delta < \Delta_c$, $\Delta = \Delta_c$, $\Delta > \Delta_c$ for the case in which $\gamma_3 = 0$ (no trigonal warping) is shown in Fig. 3.3. The white lines show the plasmon dispersion, the black solid (dashed) lines show the boundaries of the intraband (interband) particle-hole continuum. We see that as Δ crosses Δ_c the dispersion of the plasmon mode outside the particle-hole continuum doesn't change substantially. The plasmon mode inside the particle hole-continuum on the other hand is qualitatively different for $\Delta < \Delta_c$ and $\Delta > \Delta_c$, an effect that is not captured by the 2-band model [65].

In the presence of trigonal warping $\epsilon(\mathbf{q}, \omega)$ becomes strongly anisotropic and this is particularly evident when the Fermi energy cuts the sombrero region. Fig. 3.4 shows the results for $\epsilon(\mathbf{q}, \omega)$ for different directions of $\mathbf{q}$ obtained taking into account trigonal warping. From the figure the strong anisotropy of $\epsilon(\mathbf{q}, \omega)$ when $\gamma_3 \neq 0$ is evident. In particular, we see that the plasmon dispersion inside the p-h continuum has a strong dependence on the direction of $\mathbf{q}$.

For the case with no trigonal warping in the long-wavelength limit $q \ll \omega/v_F$ using

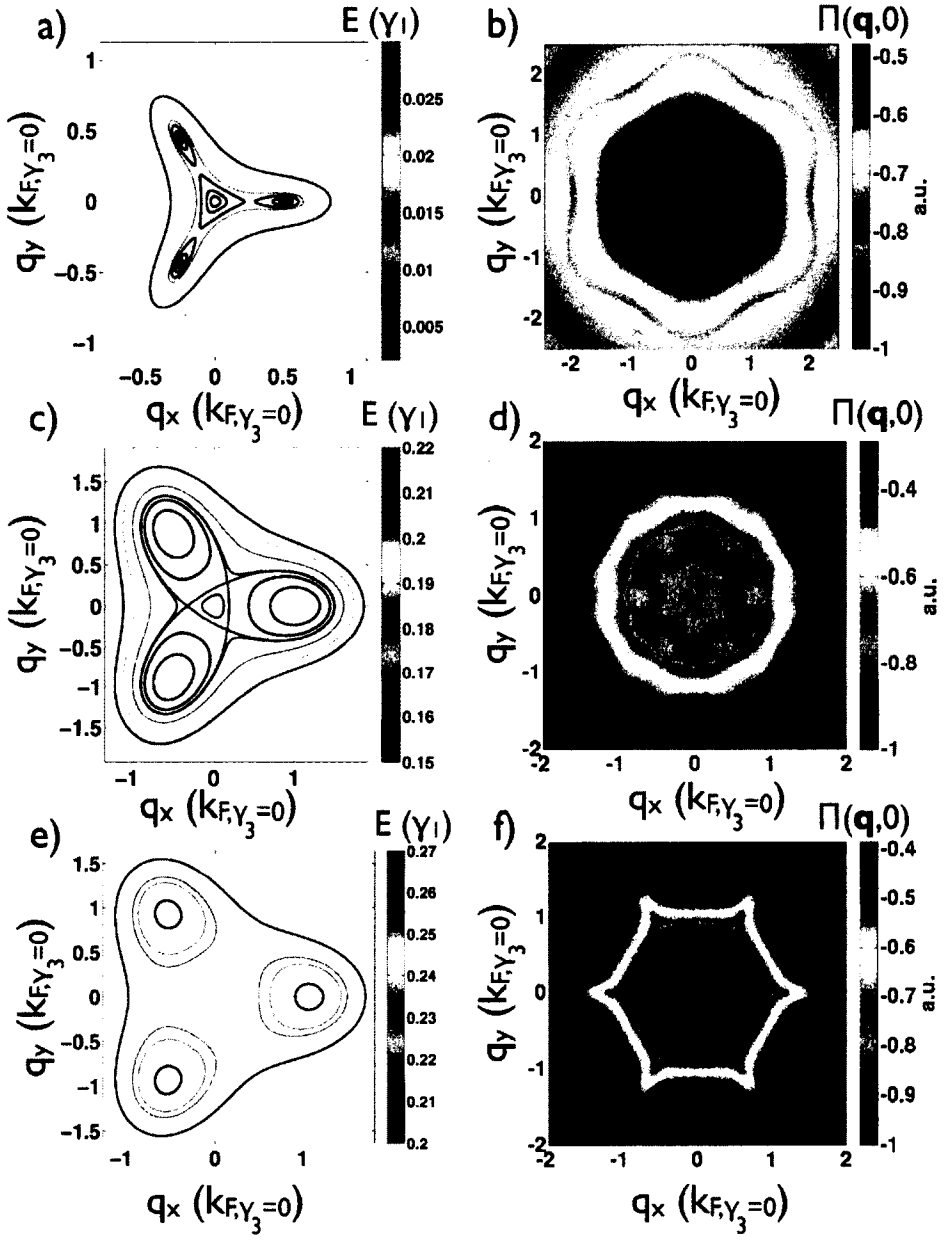

FIG. 3.2: Fermi surface and polarizability for gapped bilayer graphene with trigonal warping. (Left Column) Equipotential lines for the lowest energy band within the 4 band model with trigonal warping $\gamma_3 = 3\gamma_1/4$ and $\Delta = 0,\ 1/3\gamma_1,\ 1/2\gamma_1$ from top to bottom. (Right Column) Polarizability for $n = 10^{12}$ cm^{-2}, trigonal warping $\gamma_3 = 3\gamma_1/4$, and $\Delta = 0,\ 1/3\gamma_1,\ 1/2\gamma_1$ from the top panel to bottom one. $k_{F,\gamma_3=0}$ is k_{F+} in the limit $\gamma_3 = 0$.

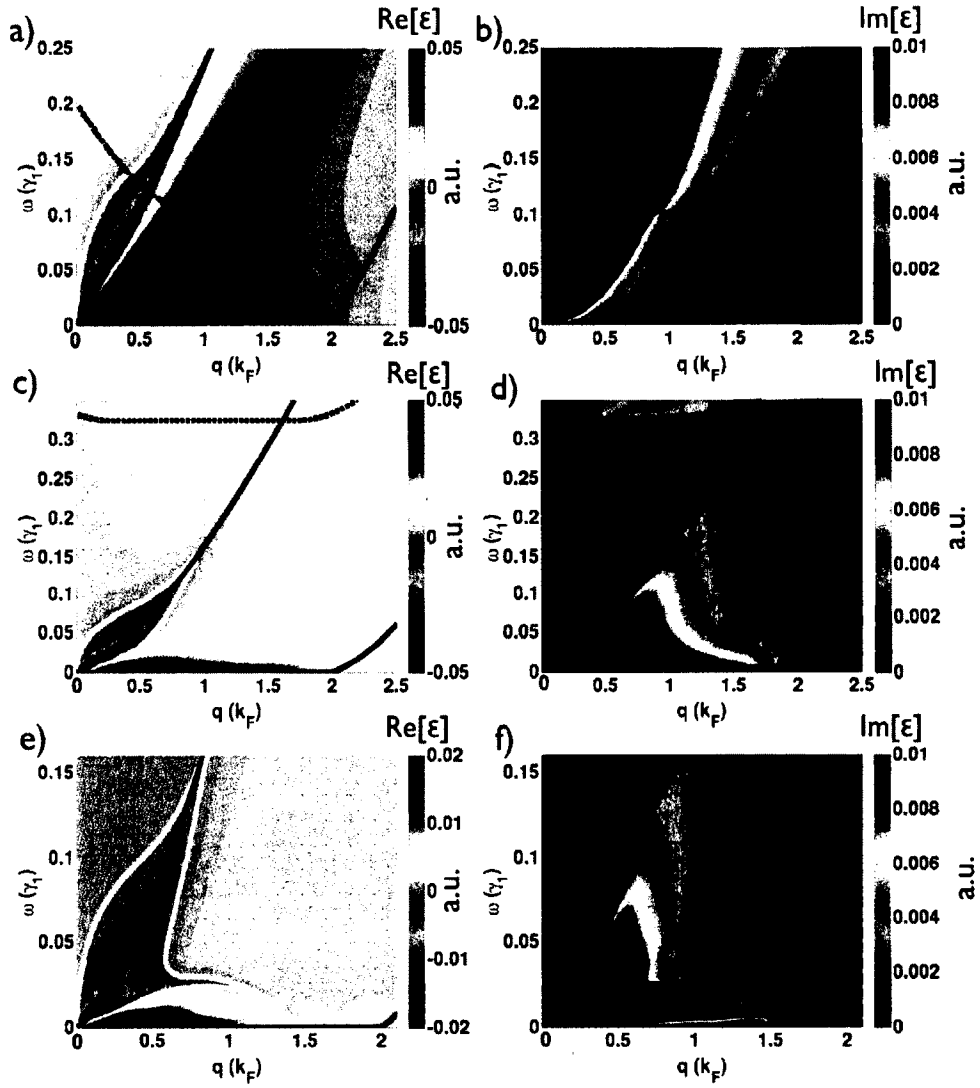

FIG. 3.3: RPA dielectric function for gapped bilayer graphene. The left (right) column shows the real (imaginary) part of $\epsilon_{\mathrm{RPA}}(\mathbf{q},\omega)$ for $\Delta = 0$, $\Delta = \gamma_1/3$, $\Delta = \gamma_1/2$ from top to bottom. The plasmon dispersion is denoted by white curves. The boundaries for the intraband (interband) particle-hole continuum are indicated with black solid (dashed) curves.

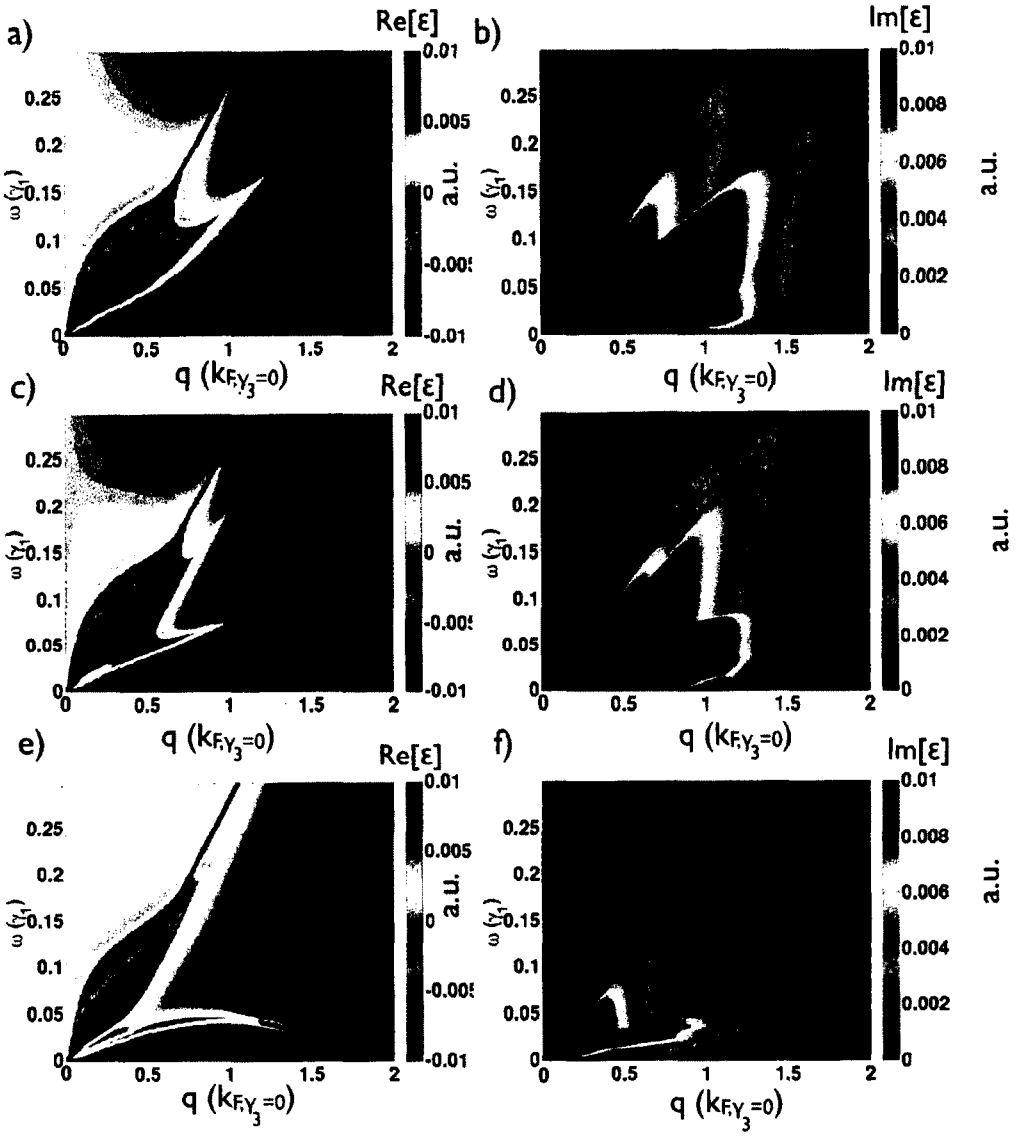

FIG. 3.4: RPA dielectric function for bilayer graphene with trigonal warping. With trigonal warping the dielectric function is anisotropic in momentum. To exhibit the anisotropy we present plots along straightline paths with different angles relative to the k_x-axis: $\theta = 0°, 15°, 30°$ (top to bottom). The left (right) column shows the real (imaginary) part of $\epsilon_{\rm RPA}(\mathbf{q},\omega)$ with $\Delta = \gamma_1/2$. The white curves denote the plasmon dispersion, the black curves denote the boundaries of the particle-hole continuum. $k_{F,\gamma_3=0}$ is k_{F+} in the limit $\gamma_3 = 0$.

the 4-band model for the polarizability, up to order q^2, we have:

$$\Pi(\mathbf{q},\omega) = \frac{gq^2}{4\pi\omega^2}\left[k_{F+}\left.\frac{\partial\epsilon_{\mathbf{k}}}{\partial\mathbf{k}}\right|_{k_{F+}} - k_{F-}\left.\frac{\partial\epsilon_{\mathbf{k}}}{\partial\mathbf{k}}\right|_{k_{F-}}\right] \tag{3.3}$$

We notice that in Eq. 3.3 there is a term proportional to k_{F-} that is absent in the 2-band model. Replacing this expression in the equation for the RPA $\epsilon(\mathbf{q},\omega)$ we find the plasmon dispersion:

$$\omega = \left[\frac{g}{2}\hbar v_F \alpha q\left(k_{F+}\left.\frac{\partial\epsilon_{\mathbf{k}}}{\partial\mathbf{k}}\right|_{k_{F+}} - k_{F-}\left.\frac{\partial\epsilon_{\mathbf{k}}}{\partial\mathbf{k}}\right|_{k_{F-}}\right)\right]^{1/2}. \tag{3.4}$$

This dispersion is general and valid both for $n < n_c$ and $n > n_c$; however, in the latter case $k_{F-} = 0$. From Eq. 3.4 using the appropriate expressions for k_{F+}, k_{F-} and $\epsilon_{\mathbf{k}}$ we find

$$\omega(q) = \sqrt{\frac{qge^2\gamma_1^2}{\epsilon_F\epsilon}}F(\hat{n},\hat{\Delta}) \tag{3.5}$$

where $\hat{n} \equiv \hbar^2 v_F^2 \pi n/\gamma_1^2$, $\hat{\Delta} \equiv \Delta/\gamma_1$, with the Fermi energy, ϵ_F, and functions $F(\hat{n},\hat{\Delta})$ given by:

2-band model:

$$F(\hat{n},\hat{\Delta}) = \hat{n}$$

$$\epsilon_F = \gamma_1[\hat{n}^2 + \hat{\Delta}^2/4]^{1/2}$$

4-band model

$$F(\hat{n},\hat{\Delta}) = \sqrt{\frac{\hat{n}}{2}\frac{\sqrt{1+4\hat{n}(1+\hat{\Delta}^2)} - (1+\hat{\Delta}^2)}{\sqrt{1+4\hat{n}(1+\hat{\Delta}^2)}}}$$

$$\epsilon_F = \frac{\gamma_1}{2}\sqrt{2+\hat{\Delta}^2+4\hat{n} - 2\sqrt{1+4\hat{n}(1+\hat{\Delta}^2)}}$$

4-band model (sombrero region)

$$F(\hat{n},\hat{\Delta}) = \frac{1}{2}\sqrt{\hat{n}\frac{\hat{\Delta}^4+2\hat{\Delta}^2-\hat{n}^2}{\hat{\Delta}^4+2\hat{\Delta}^2-\hat{n}^2+1}}$$

$$\epsilon_F = \frac{\gamma_1}{2}\sqrt{\frac{\hat{n}^2+\hat{\Delta}^2}{1+\hat{\Delta}^2}}.$$

In Fig. 3.5 (a) we compare the results for the plasmon dispersion obtained numerically using the 4-band model with the ones given by Eq. 3.5 using $\Delta = \gamma_1/2$ for a given value

of n. Following the overall theme of this chapter, we see that the 2-band results differ substantially from the 4-band results. At low densities ($n < n_c$) this is due to the fact that the 2-band model does not capture the nonmonotonic band structure, i.e. the fact that in the 2-band model in Eq. 3.4 there is no term $k_{F-}\partial\epsilon_{\mathbf{k}}/\partial\mathbf{k}|_{k_{F-}}$. For $n > n_c$ this is due to the fact that in the 4-band model the dispersion is closer to linear than parabolic as it is in the 2-band model, in analogy to what happens in the gapless case [61]. This is summarized in Fig. 3.5 (b) that shows the ratio $\omega_{4-\text{band}}/\omega_{2-\text{band}}$ between the plasmon frequency obtained within the 4-band and the 2-band model as a function of n for different values of Δ. Notice, that in the long-wavelength limit this ratio (see Eq. 3.5) is independent of q and is a function only of n and Δ.

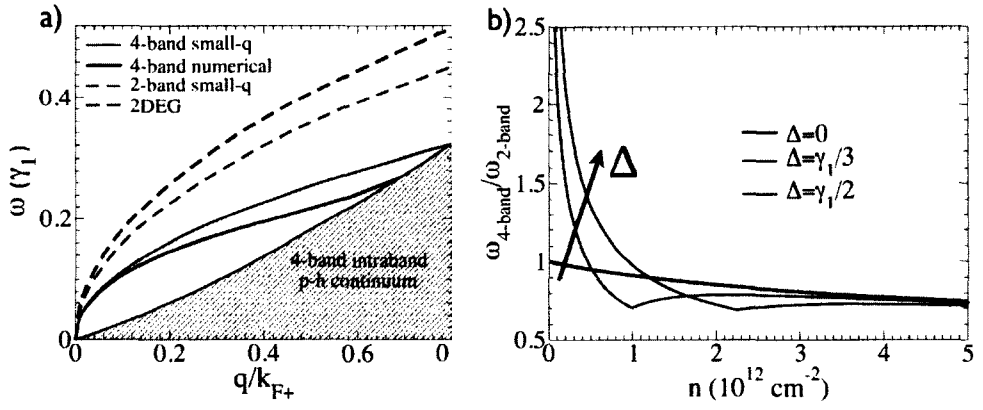

FIG. 3.5: Long wavelength plasmon dispersion for gapped bilayer graphene. (a) Comparison of the plasmon dispersion for $\Delta = \gamma_1/2$ obtained using the full 4-band model, and the 2-band model for $n = 2.7 \times 10^{12}\text{cm}^{-2}$ (b) Ratio $\omega_{4-\text{band}}/\omega_{2-\text{band}}$ as a function of doping for different value of Δ. For $\Delta \neq 0$ and $n \to 0$ the ratio $\omega_{4-\text{band}}/\omega_{2-\text{band}}$ diverges.

3.3 Summary

In this chapter we studied the static and dynamic screening of gapped bilayer graphene using the full 4-band model. We found that the static screening obtained using the 4-

band model is qualitatively different from the one obtained from the 2-band model. In particular in the 4-band model, when the gap is nonzero, the static polarizability exhibits Kohn anomalies not present in the 2-band model. For the dynamic screening we found that the plasmon frequency within the 4-band model is substantially different from the one obtained within the 2-band model especially at low densities when $\Delta \neq 0$. We also characterized the strong anisotropic properties of the static and dynamic screening due to the trigonal warping. We found that in the presence of trigonal warping in gapped graphene the number of Kohn anomalies depends not only on the doping and the band-gap but also on the direction of the momentum. Our results, in particular the identification of additional Kohn anomalies, and the strong anisotropic nature of the screening in the presence of trigonal warping, have important implications for understanding of the phonon spectrum and the nature of the RKKY interaction in gapped bilayer graphene, and are therefore expected to have clear experimental signatures. Moreover our results also apply to the case in which a gap opens due to the realization of a spontaneously broken symmetry state and could then be used to identify and characterize such a state.

CHAPTER 4

Proximity Effect in Graphene-Topological Insulator Heterostructures

This chapter is based on the work from [66]. As discussed in Chapter 2, the surface of strong three-dimensional (3D) topological insulators (TIs) [30] and graphene [9, 10] have a very similar low-energy electronic structure in that the conduction and the valence bands touch at isolated points, the Dirac points (DPs), and around these points the fermionic excitations are well described as massless two-dimensional (2D) chiral Dirac fermions for which the phase of a two-state quantum degree of freedom is locked with the momentum direction. However, there are also important differences between these materials. One important difference is that in TIs the electron-phonon scattering is much stronger than in graphene, which can decrease the carrier mobility in contrast to graphene which has the highest room-temperature mobility of any known material. Another major difference is that in graphene the chirality is associated with the sublattice degree of freedom in contrast

to the TI surface (TIS) in which it is associated with the intrinsic electron spin and caused by strong spin-orbit (SO) coupling. Heuristically, one might expect that proximity to the TIS could enhance the SO coupling of graphene thus creating a novel 2D system with non-trivial spin textures and high, room-temperature, electron mobility. This approach to enhance the SO coupling in graphene appears to be more practical than previously proposed approaches [67, 68] that rely on doping graphene with heavy adatoms. These facts, together with recent experimental progress in manufacturing heterostructures [69, 70] motivated us to study graphene-TI heterostructures.

In what follows we study the low-energy electronic properties of heterostructures formed by graphene placed on the conducting surface of a 3D TI. As we will show, not only does the proximity of a TIS enhance the SO coupling in graphene, and bilayer graphene (BLG), but this enhancement can be controlled via a relative twist between the graphene lattice and the TIS lattice. The presence of a relative rotation typically induces an incommensurate stacking of the graphene and the substrate [40, 41, 71–100]. As a consequence we develop and present a theory that is able to take into account the incommensurability between graphene and the TIS. This is difficult to achieve via standard approaches, like density functional theory (DFT) [101], and tight-binding models, due to the computational cost of these approaches for incommensurate structures. A continuum model, on the other hand, can effectively treat heterostructures with incommensurate stacking. To develop the theory for incommensurate structures; however, we need a continuum model for the commensurate limit. Thus, we will first present such a model and then, starting from it, derive a model able to treat incommensurate graphene-TI structures. Our results show that in graphene-TI heterostructures the proximity effect induces a strong enhancement of the SO coupling in graphene, non-trivial spin and pseudospin textures on the bands, and that all these effects can be tuned to great extent via the relative rotation between graphene and the TI. Moreover, we present results for the case in which tunneling processes with finite

momentum transfer are present.

4.1 Basic Considerations

We consider the TI material to be a Tetradymite such as Bi_2Se_3, Bi_2Te_3, and Sb_2Te_3. The projected surface Brillouin zone (BZ) is hexagonal with a single DP at the zone center [32]. Let a_2 be the effective lattice constant that corresponds to the surface BZ and $a_1 = 2.46\mathring{A}$ the graphene lattice constant. Defining the ratio $a_2/(\sqrt{3}a_1) \equiv 1 + \delta$ we have $\delta < 0.01$ for Sb_2Te_3 and $\delta \approx -0.03\%$ ($\delta \approx 0.03\%$) for Bi_2Se_3 (Bi_2Te_3). Thus, the study of the commensurate $\sqrt{3} \times \sqrt{3}$ stacking pattern is expected to be a good approximation for a graphene-Sb_2Te_3 heterostructure and for developing the theory for incommensurate structures. The Hamiltonian describing the electronic degrees of freedom of the heterostructure can be written as $H = H^{\mathrm{g}} + H^{\mathrm{TIS}} + H_t$, where H^{g} is the Hamiltonian for an isolated sheet of graphene, H^{TIS} is the Hamiltonian for the TIS, and H_t describes tunneling processes between graphene and the TIS. As we discussed in Chapter 2 the long wavelength physics of graphene is described by a pair of 2D massless Dirac Hamiltonians:

$$H^{\mathrm{g},K} = \sum_{\mathbf{p},\sigma,\tau\tau'} c^{\dagger}_{\mathbf{K}+\mathbf{p},\tau,\sigma} \left(\hbar v_1 \boldsymbol{\tau} \cdot \mathbf{p} - \mu_1\right)_{\tau\tau'} c_{\mathbf{K}+\mathbf{p},\tau',\sigma}$$

and

$$H^{\mathrm{g},K'} = \sum_{\mathbf{p},\sigma,\tau\tau'} c^{\dagger}_{\mathbf{K}'+\mathbf{p},\tau,\sigma} \left(\hbar v_1 \boldsymbol{\tau}^* \cdot \mathbf{p} - \mu_1\right)_{\tau\tau'} c_{\mathbf{K}'+\mathbf{p},\tau',\sigma}$$

where $c^{\dagger}_{\mathbf{K}+\mathbf{p},\tau,\sigma}$ ($c_{\mathbf{K}+\mathbf{p},\tau,\sigma}$) creates (annihilates) a Dirac fermion on sublattice τ (A, B) with spin σ ($\uparrow, \downarrow$) at a Dirac wave vector $\mathbf{p}$ measured from one of the two inequivalent BZ corners (K- and K'-valley) located at wave vectors $\mathbf{K}$ and $\mathbf{K}'$ ($|\mathbf{p}| \ll |\mathbf{K}|$), $\boldsymbol{\tau} = \begin{pmatrix} \tau^x, & \tau^y \end{pmatrix}$ are Pauli matrices acting on the sublattice space, $v_1 \approx 10^6$m/s is the Fermi velocity, and μ_1

is the chemical potential. The TIS states near its Dirac point can be described by an effective 2D continuum model [32, 33]:

$$H^{\mathrm{TIS}} = \sum_{\mathbf{k},\sigma\sigma'} a^{\dagger}_{\mathbf{k},\sigma} \left[\hbar v_2 \left(\boldsymbol{\sigma} \times \mathbf{k}\right) \cdot \hat{\mathbf{z}} - \mu_2\right]_{\sigma\sigma'} a_{\mathbf{k},\sigma'}$$

where $a^{\dagger}_{\mathbf{k},\sigma}$ ($a_{\mathbf{k},\sigma}$) creates (annihilates) a surface massless Dirac fermion with spin σ at wave vector $\mathbf{k}$ measured from the zone center ($\overline{\Gamma}$-point), $\boldsymbol{\sigma} = \begin{pmatrix} \sigma^x, & \sigma^y \end{pmatrix}$ are Pauli matrices acting on spin space, $\hat{\mathbf{z}}$ is the unit vector along the z direction, and μ_2 is the chemical potential. In Bi_2Se_3, Bi_2Te_3, and Sb_2Te_3, the Fermi velocity v_2 is roughly half of that in graphene, hence in the remainder of this chapter we assume $v_2 = v_1/2$. In our model we neglect the hexagonal warping of the TIS bands due to higher order terms in k in H^{TIS} [102]. Such effects are only important at relatively high energies $\gtrsim 200$ meV away from the TI's DP [102, 103] and we are only interested in the energy range close to the TI's DP. We also neglect effects due the TI's bulk states [104] for two reasons: (i) in current experiments the effect of the bulk states can be strongly suppressed via chemical and field effect doping [103, 105–107], and by using TI thin films [108, 109]; (ii) the most interesting situation arises when the bulk states can be neglected: in this case the properties of the systems are dominated not by the TI's bulk states but by the states resulting from the hybridization of the graphene and the TI's surface states. The form of H_t depends on the stacking pattern and the interface properties as we show below.

4.2 Commensurate Stacking

We first consider the graphene-TI heterostructure in a $\sqrt{3} \times \sqrt{3}$ commensurate stacking, in which each TIS atom is directly underneath a carbon atom. The strongest tunneling is expected to occur between the directly stacked atoms, among which all the carbon atoms

can be shown to belong to one sublattice. For concreteness, we will choose this to be the A sublattice. As a result of the periodic tunneling potential, in the BZ of the heterostructure the original graphene BZ is folded such that the two valleys are both located at the zone center overlapping with the DP of the TIS, Fig. 4.1 (a), (b). In this case the tunneling Hamiltonian can be written as $H_t = \sum_{\mathbf{k},\lambda,\tau,\sigma} t_\tau a^\dagger_{\mathbf{k},\sigma} c_{\lambda,\mathbf{k},\tau,\sigma}$ + h.c., where $\lambda = K, K'$ and the tunneling matrix elements $t_A = t$, $t_B = 0$ are assumed to be spin and momentum independent. The Hamiltonian for such a structure takes the form

$$\hat{\mathcal{H}}_{\mathbf{k}} = \begin{pmatrix} \hat{H}^{g,K}_{\mathbf{k}} & 0 & \hat{T}^\dagger \\ 0 & \hat{H}^{g,K'}_{\mathbf{k}} & \hat{T}^\dagger \\ \hat{T} & \hat{T} & \hat{H}^{\mathrm{TIS}}_{\mathbf{k}} \end{pmatrix}, \quad \hat{T} = \begin{pmatrix} t & 0 & 0 & 0 \\ 0 & 0 & t & 0 \end{pmatrix}, \tag{4.1}$$

where the graphene blocks are 4×4 matrices in sublattice and spin space whereas the TIS block is a 2×2 matrix in spin space.

We can gain some insight using a perturbative approach [110]. In this approach the effect of tunneling processes on the graphene spectrum is captured by the self-energy $\hat{\Sigma}_{\mathbf{k}}(i\omega_n) = \hat{V}^\dagger \hat{G}^0_{\mathbf{k}}(i\omega_n)\hat{V}$, where $\hat{G}^0_{\mathbf{k}}(i\omega_n)$ is the Green's function of the TIS and $\hat{V}$ is the tunneling vertex. In the basis formed by the eigenstates of the Hamiltonian of isolated graphene, $\Phi_{\lambda,\mathbf{k},\alpha,\sigma}$, where $\alpha = \pm$ refer to the 4-fold degenerate upper and lower bands we obtain

$$\hat{\Sigma}_{\mathbf{k}}(i\omega_n) = \begin{pmatrix} \Sigma^S_{\mathbf{k}}(i\omega_n) & e^{-i\left(\theta_{\mathbf{k}}-\frac{\pi}{2}\right)}\Sigma^A_{\mathbf{k}}(i\omega_n) \\ e^{i\left(\theta_{\mathbf{k}}-\frac{\pi}{2}\right)}\Sigma^A_{\mathbf{k}}(i\omega_n) & \Sigma^S_{\mathbf{k}}(i\omega_n) \end{pmatrix} \otimes (\mathrm{I}_\alpha + \sigma^x_\alpha) \otimes (\mathrm{I}_\lambda + \sigma^x_\lambda), \tag{4.2}$$

where $\Sigma^{S/A}_{\mathbf{k}}(i\omega_n) = (t^2/2)\, G^{S/A}_{\mathbf{k}}(i\omega_n)$ with $G^{S/A}_{\mathbf{k}}(i\omega_n) = \left[\frac{1}{(i\omega_n - \hbar v_2 k + \mu_2)} \pm \frac{1}{(i\omega_n + \hbar v_2 k + \mu_2)}\right]/2$, and the first 2×2 matrix acts in the spin space, $(\mathrm{I}_\alpha + \sigma^x_\alpha)$ acts in the band space, and

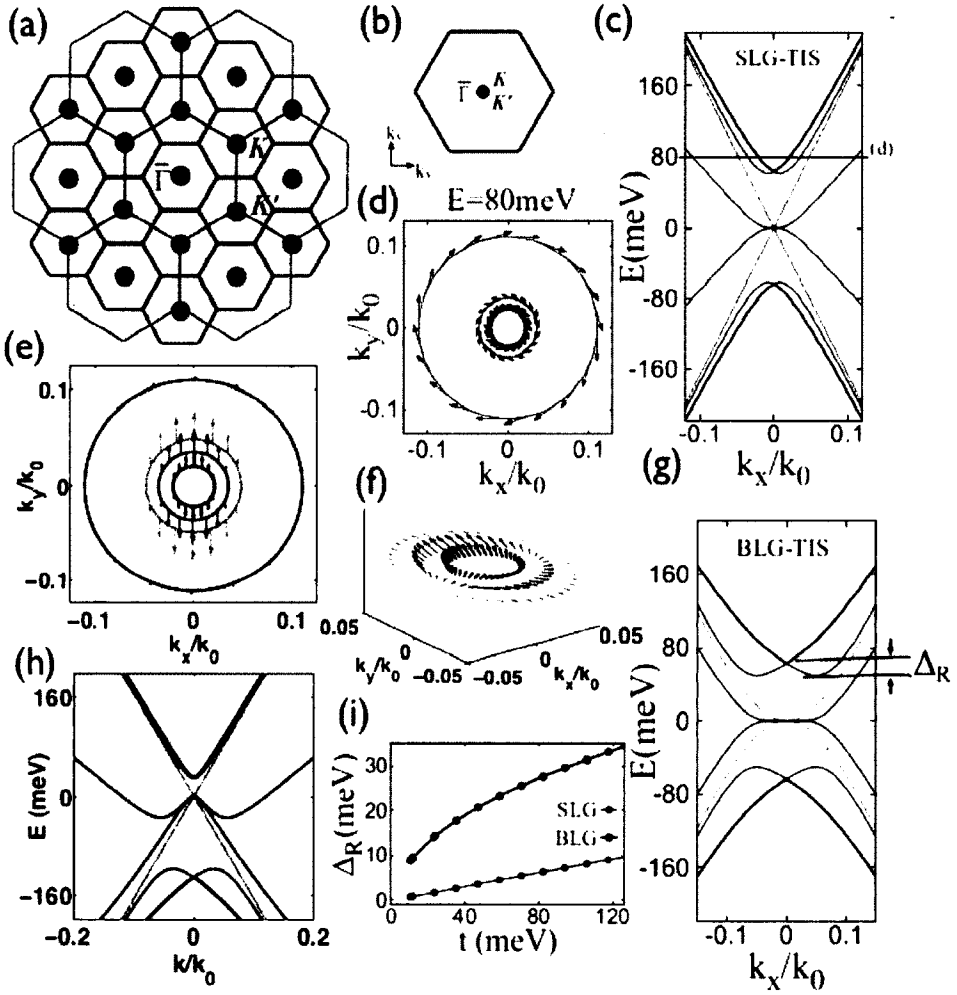

FIG. 4.1: Schematic of stacked graphene-topological insulator heterostructure and electronic structure for commensurate stacking. (a) Schematics of the $\sqrt{3}\times\sqrt{3}$ stacked graphene BZ (dark) and TIS BZ (light) in the repeated zone scheme without tunneling. (b) Folded BZ after turning on tunneling. (c) Renormalized bands of SLG-TIS for $\mu_1 = \mu_2 = 0$. Here $k_0 \equiv 830\text{meV}/(\hbar v_2)$. (d) Spin texture on the bands at $E = 80$ meV. The arrows indicate spin directions. (e) Texture of the in-plane component of the pseudospin at $E = 80$ meV, (f) shows the full pseudospin orientation on the three Fermi surfaces closest to the $\bar{\Gamma}$ point. (g) Renormalized bands of BLG-TIS. (h) Renormalized bands of SLG-TIS for $\mu_1 = 0$, $\mu_2 = 100$ meV. (i) Rashba-like splitting Δ_R in SLG-TIS and BLG-TIS as a function of t.

$(\mathrm{I}_\lambda + \sigma_\lambda^x)$ in the valley space. I is the 2×2 identity matrix and $\theta_{\mathbf{k}} = \arctan(k_y/k_x)$. The appearance of non-zero off-diagonal spin components with phase factor $\left(\theta_{\mathbf{k}} - \frac{\pi}{2}\right)$ in the self-energy indicates an induced helical spin texture on some of the graphene bands.

We can also obtain the eigenvalues and eigenstates of the model numerically by diagonalizing Eq. 4.1. In this case we find that the renormalized graphene bands in the perturbative approach coincide with those obtained by direct diagonalization. Figure 4.1(c) shows the band structure of a graphene-TI heterostructure with $t = 45\,\mathrm{meV}$ and $\mu_1 = \mu_2 = 0$. We see that the fourfold degeneracy of the original graphene bands is partially lifted in Fig. 4.1 (c). It appears that two pairs of graphene-like bands become gapped and split (blue and red) while two other pairs of graphene bands appear to remain unchanged and the TI-like bands (green) simply develop a less linear behavior at low energies. It can be shown that the seemingly unchanged graphene bands are in fact orthogonal linear combinations of the graphene states from the K and K' points. The most explicit way to show this is by noting that the matrix in Eq. 4.1 can be block diagonalized into two uncoupled blocks:

$$\hat{\mathcal{H}}'_{\mathbf{k}} = \begin{pmatrix} \hat{H}^{\mathrm{g},K}_{\mathbf{k}} & 0 & 0 \\ 0 & \hat{H}^{\mathrm{g},K}_{\mathbf{k}} & \sqrt{2}\hat{T}^\dagger \\ 0 & \sqrt{2}\hat{T} & \hat{H}^{\mathrm{TIS}}_{\mathbf{k}} \end{pmatrix}. \tag{4.3}$$

Thus making the origin of the band structure more apparent. Note that the uncoupled graphene Hamiltonian appearing in Eq. 4.3 actually emerges from a unitary transformation which mixes the two valleys. A different choice of unitary transformation would result in a block that was identical to $\hat{H}^{\mathrm{g},K'}_{\mathbf{k}}$ instead of $\hat{H}^{\mathrm{g},K}_{\mathbf{k}}$.

Using the eigenstates obtained through direct diagonalization both the spin and pseudospin configurations may be computed on the renormalized bands, Fig. 4.1 (d)-(f). We can see from Fig. 4.1 (d) that, as we suspected from the form of the self-energy, the in-plane spin on the two gapped bands (forming the two smaller Fermi surfaces) is locked

perpendicular to the momentum, winding around the $\overline{\Gamma}$ point analogous to a system with Rashba-type SO coupling. These bands seem to be the spin-split descendants of the spin degenerate graphene bands with one band's spin winding clockwise and the other winding counterclockwise. Notice that after coupling to the TIS the graphene bands have a unique pseudospin structure very different from the pseudospin structure of both the original K and K' valley, shown in Fig. 4.1 (e) and (f). This makes sense considering the fact that the graphene states which hybridize with the TIS are actually linear combinations of states from the K and K' valleys. This should affect transport measurements in a unique way.

Our model is easily generalized to the case of BLG. One simply needs to replace the graphene Hamiltonian with the bilayer graphene Hamiltonian. The results for a BLG-TI heterostructure, Fig. 4.1 (g), shows a similar trend to the results for a SLG-TI heterostructure. However, as shown in Fig. 4.1 (i), the proximity-induced enhancement of the SO coupling in BLG is much larger than in single layer graphene (SLG). This could be a consequence of the fact that, at low energies, BLG has a much higher density of states (DOS) than SLG.

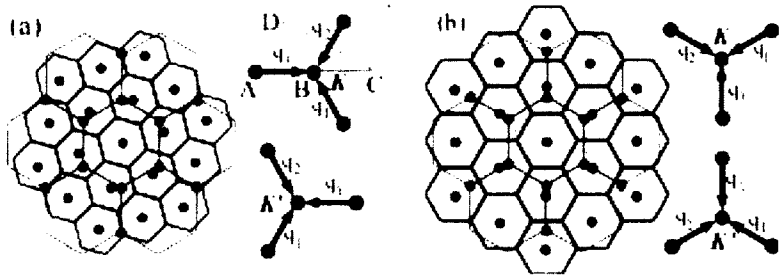

FIG. 4.2: Schematic of incommensurate stacked graphene-topological insulator heterostructure. Schematic of the graphene and TIS BZs in an incommensurate structure formed from (a) a twist (b) a lattice mismatch, with the corresponding $\mathbf{q}_j$ vectors at the K- and K'-point.

Within our model we can easily account for a difference $\delta\mu = \mu_2 - \mu_1$ between the TI and graphene chemical potential. By varying $\delta\mu$ the value of $\mathbf{k}$ for which the pristine

bands of the TI and graphene cross, and for which the hybridization is stronger, can be tuned. Fig. 4.1 (h) shows the case for which $\mu_2 = 100$ meV and $\mu_1 = 0$. We see that in this case the induced Rashba splitting is stronger than when $\mu_2 = \mu_2 = 0$. This is consistent with the fact that the DOS increases as we move away from the DP.

4.3 Incommensurate Stacking

We now consider incommensurate structures. In general, the tunneling matrix elements can be written as:

$$T_\tau(\mathbf{k}_2, \mathbf{k}_1) = \sum_{\mathbf{G}_1, \mathbf{G}_2} \frac{t(\mathbf{k}_1 + \mathbf{G}_1)}{\sqrt{3}\Omega_1} e^{i\mathbf{G}_1 \cdot \mathbf{d}_\tau} \delta_{\mathbf{k}_2 + \mathbf{G}_2, \mathbf{k}_1 + \mathbf{G}_1} \tag{4.4}$$

where the crystal momentum is conserved by the tunneling process in which a graphene quasiparticle of wave vector $\mathbf{k}_1$ residing on sublattice τ hops to a TIS state with wave vector $\mathbf{k}_2$. Ω_1 is the graphene unit cell area and $\mathbf{d}_A = \mathbf{0}$, $\mathbf{d}_B = \begin{pmatrix} -a_0, & 0 \end{pmatrix}$ are the positions of the two carbon atoms in a unit cell with carbon-carbon distance a_0. $\{\mathbf{G}_1\}, \{\mathbf{G}_2\}$ are the reciprocal lattice vectors of graphene and TIS, respectively. $t(\mathbf{k})$ are the Fourier amplitudes of the tunneling potential $t(\mathbf{r})$ assumed to be a smooth function of $\mathbf{r}$, the spatial separation between graphene and TIS atoms projected onto the interface plane. Given that the graphene-TIS separation distance exceeds the inter-atomic distance in each material, the dominant tunneling amplitudes of $t(\mathbf{k})$ near the graphene DP are the ones with $|\mathbf{k}| = K_D \equiv |\mathbf{K}|$. This justifies a restriction of the sum over $\{\mathbf{G}_1\}$ to three vectors: $\mathbf{g}_1 (= \mathbf{0})$, $\mathbf{g}_2$, $\mathbf{g}_3$, where the latter two connect a valley with its equivalent first BZ corners. Thus, for small wave vectors measured from the respective DPs, we have

$$H_t = \sum_{\mathbf{p}, \tau, \sigma} \sum_{j,l,\cdots=1}^{3} [T_{\tau,j} a^\dagger_{\mathbf{p}+\mathbf{q}_j,\sigma} c_{\mathbf{p},\tau,\sigma} + T^*_{\tau,l} c^\dagger_{\mathbf{p}+\mathbf{q}_j+\bar{\mathbf{q}}_l,\tau,\sigma} a_{\mathbf{p}+\mathbf{q}_j,\sigma} + \dots]$$

where $T_{\tau,j} = t' e^{i\mathbf{g}_j \cdot \mathbf{d}_\tau}$ with $t' \equiv t(K_D)/\left(\sqrt{3}\Omega_1\right)$, $\{\mathbf{q}_j\}$ are the offset vectors between the graphene DP and the three "nearest-neighbouring" TIS DPs, and $\bar{\mathbf{q}}_l \in \{-\mathbf{q}_j\}$, as shown in Fig. 4.2. The repeated action of this "nonlocal" coupling generates a k-space lattice [86]. For a rotation angle θ, the separation between the offset DPs is $|\mathbf{q}_j| \equiv q = 2K_D \sin(\theta/2)$, for the lattice mismatch $q = |\delta/(1+\delta)|\, K_D$, Fig. 4.2.

For very small twist angles or lattice mismatches such that the dimensionless parameter $\gamma \equiv \frac{t'}{\hbar v_2 q} > 1$, graphene and TIS will be strongly coupled. However, when $\gamma < 1$, a weak coupling theory is valid [78, 86, 88]. In this case, to investigate the low-energy spectrum of graphene, we can truncate the k-space lattice and use the effective Hamiltonian:

$$\hat{\mathcal{H}}_{\mathbf{p}} = \begin{pmatrix} \hat{H}^{g,K}_{\mathbf{p}} & \hat{T}_1^\dagger & \hat{T}_2^\dagger & \hat{T}_3^\dagger \\ \hat{T}_1 & \hat{H}^{\mathrm{TIS}}_{\mathbf{q}_1+\mathbf{p}} & 0 & 0 \\ \hat{T}_2 & 0 & \hat{H}^{\mathrm{TIS}}_{\mathbf{q}_2+\mathbf{p}} & 0 \\ \hat{T}_3 & 0 & 0 & \hat{H}^{\mathrm{TIS}}_{\mathbf{q}_3+\mathbf{p}} \end{pmatrix}, \tag{4.5}$$

$$\hat{T}_1 = \begin{pmatrix} t' & t' & 0 & 0 \\ 0 & 0 & t' & t' \end{pmatrix}, \; \hat{T}_2 = \begin{pmatrix} t' & t'e^{-i\frac{2\pi}{3}} & 0 & 0 \\ 0 & 0 & t' & t'e^{-i\frac{2\pi}{3}} \end{pmatrix},$$

$$\hat{T}_3 = \begin{pmatrix} t' & t'e^{i\frac{2\pi}{3}} & 0 & 0 \\ 0 & 0 & t' & t'e^{i\frac{2\pi}{3}} \end{pmatrix}.$$

where $t' = t/3$. A similar Hamiltonian is valid for the K'-valley [111].

Figures 4.3 (a)-(c) show the band and spin structure around the K-point for an incommensurate graphene-TI heterostructure with $\gamma = 0.2$, $t' = 15\,\mathrm{meV}$ and $\mu_1 = \mu_2 = 0$. The result for the K'-point is simply a 60° rotation of the result for the K-point. As we can see in Fig. 4.3 the original twofold spin degeneracy of the graphene Dirac cone is completely lifted. Furthermore, of the two original degenerate linear bands one is now fully gapped and the other is no longer linear at the DP. Moreover, the bands acquire non-trivial in-

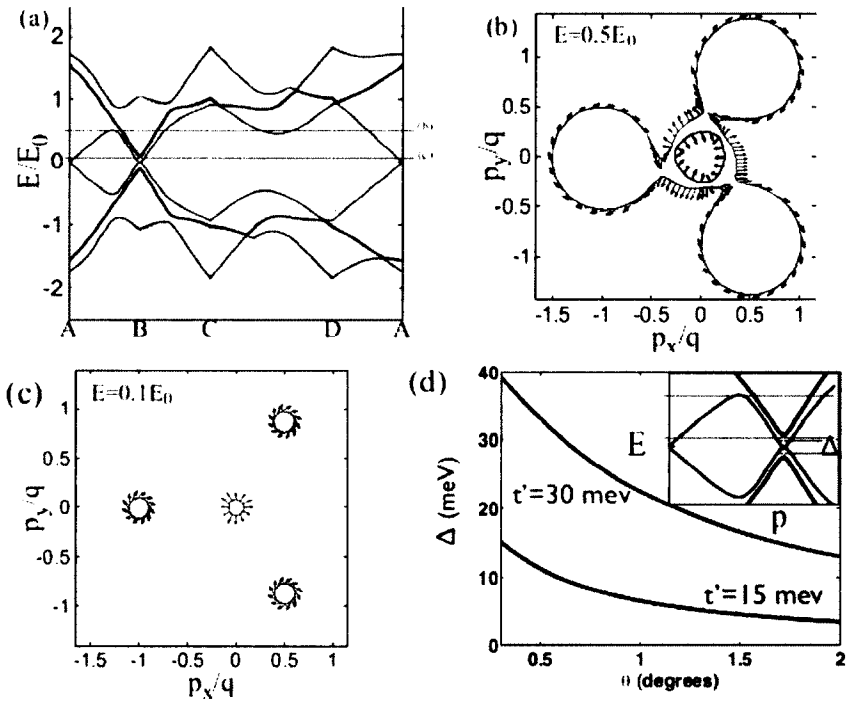

FIG. 4.3: Electronic structure for incommensurate stacked graphene-topological insulator heterostructure. Splitting of the bands can be tuned with relative twist angle. (a) The band structure along the path A-B-C-D-A indicated in Fig. 4.2(a). (b),(c) show the spin texture on the bands at different energies. $E_0 \equiv \hbar v_2 q = t'/\gamma$. (d) Splitting ($\Delta$) of the low-energy bands as a function of twist angle for $t' = 30$ meV and $t' = 15$ meV.

plane spin textures. An interesting characteristic of graphene-TI heterostructures is that the features of the band structure and spin texture can be controlled via the twist angle. By changing the value of θ, for fixed t and energy, the distance between the Fermi pockets shown in Fig. 4.3 (b) and (c), and their size, can be tuned. In addition, the splitting of the low energy bands Δ can be controlled as shown in Fig. 4.3 (d).

In the presence of surface roughness and/or phonons tunneling processes with finite momentum transfer are allowed. To gain some insight into their possible effect, we consider the case in which the tunneling amplitude has a Gaussian profile with respect to the momentum transfer $\mathbf{q}$: $t_{\mathbf{q}} = t_0 \exp(-|\mathbf{q}|^2/(2\sigma^2))$, where t_0 characterizes the tunneling strength and σ the variance. To qualitatively understand the effect of such processes, we study the case of an isolated graphene Dirac cone separated by a large wave vector $\mathbf{Q}$ from the closest TIS DP. Using the perturbative approach outlined above, the proximity effect on the graphene spectrum is captured by the self-energy

$$\hat{\Sigma}_{\mathbf{Q}+\mathbf{p}}(i\omega_n) = (\mathrm{I}_\alpha + \sigma_\alpha^x) \otimes \begin{pmatrix} \Sigma^S_{\mathbf{Q}+\mathbf{p}}(i\omega_n) & e^{-i(\theta_{\mathbf{Q}+\mathbf{p}}-\frac{\pi}{2})}\Sigma^A_{\mathbf{Q}+\mathbf{p}}(i\omega_n) \\ e^{i(\theta_{\mathbf{Q}+\mathbf{p}}-\frac{\pi}{2})}\Sigma^A_{\mathbf{Q}+\mathbf{p}}(i\omega_n) & \Sigma^S_{\mathbf{Q}+\mathbf{p}}(i\omega_n) \end{pmatrix} \tag{4.6}$$

with $\Sigma^{S/A}_{\mathbf{Q}+\mathbf{p}}(i\omega_n) = \frac{t_0^2\Omega_2}{2\pi} \exp\left[-\frac{|\mathbf{Q}+\mathbf{p}|^2}{\sigma^2}\right] \int_0^\infty k \exp\left[-\frac{k^2}{\sigma^2}\right] \times I_{0/1}(\frac{2|\mathbf{Q}+\mathbf{p}|}{\sigma^2}k) G^{S/A}_{\mathbf{k}}(i\omega_n)\mathrm{d}k$, where $I_n(x)$, $n = 0, 1$ are the modified Bessel functions of the first kind. The form of the phase factors in the off-diagonal spin components of $\hat{\Sigma}$ implies an induced spin texture on graphene with the spin perpendicular to the wave vector $\mathbf{Q} + \mathbf{p}$, Fig.4.4 (a). We find in this case that the spin degenerate bands are split and the remaining gapless bands are no longer linear, Fig. 4.4(b). Figures 4.4(c)-(d) show the size of the gap between spin-split bands as a function of t_0 and σ, respectively.

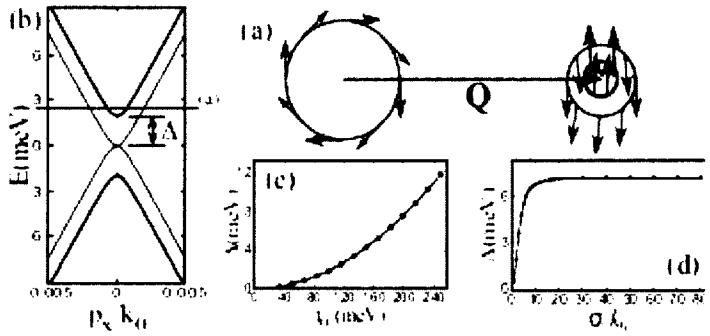

FIG. 4.4: Induced spin texture in incommensurate stacked graphene-topological insulator heterostructure considering a single Fermi pocket. (a) Schematics of the induced spin texture on graphene (right) from the TIS spin helix (left). (b) Renormalized graphene bands (solid lines) for $t_0 = 100\,\text{meV}$, $\sigma = 2k_0$, Spin-split gap (Δ) as a function of t_0 (c) and σ (d).

4.4 Summary

In conclusion, we have studied the proximity effect of a strong 3D TI on the low-energy spectrum of graphene in commensurate and incommensurate structures as well as in a case with surface roughness. To be able to take into account the incommensurability we have developed a continuous model. Using this model we identified the spin and pseudospin structure of all the hybridized bands for both commensurate and incommensurate stacking. The results indicate potential signatures in transport measurements. Additionally, we showed that the enhancement of the SO coupling is typically much stronger in BLG than graphene. We also found that these novel properties can be tuned by varying the relative rotation between the graphene and the TIS lattices.

CHAPTER 5

Effect of a Spin-Active Interface on Proximity-Induced Superconductivity

This chapter is based on work presented in [112]. As we have already seen in the previous chapters, the combination of layers of different materials, such as TIs and graphene or bilayer graphene allows the realization of new systems with novel and interesting electronic properties. There is also a great deal of interest surrounding the novel states found in heterostructures formed by interfacing a TI surface and superconductors (SCs) [113–117]. In particular, it has been shown theoretically that Majorana excitations may arise in certain TI/SC heterostructures by including ferromagnetic materials [118–121]. Additionally, it has been shown theoretically, and there is experimental evidence to suggest, that in heterostructures formed by a TI and an s-wave SC, via the proximity effect, p-wave triplet superconducting pairings can be induced in the TI's surface [114, 122]. More recently it has also been shown that the proximity of a SC to a TI could induce odd-frequency

superconducting pairing in the TI's surface [115–117].

The symmetry of a superconducting state is characterized by the symmetry properties of the pairing amplitude $F(\mathbf{r}_1, t_1; \mathbf{r}_2, t_2) = \sum_{\alpha,\beta} \langle T c_\alpha(\mathbf{r}_1, t_1) c_\beta(\mathbf{r}_2, t_2) \rangle g_{\alpha\beta}$, where $g_{\alpha\beta}$ is a metric tensor describing the spin structure of the Cooper pair. Because electrons are fermions if $g_{\alpha\beta}$ describes a spin singlet then the equal time correlation function must be even in parity $F(\mathbf{r}_1, t; \mathbf{r}_2, t) = F(\mathbf{r}_2, t; \mathbf{r}_1, t)$ and if it describes a spin triplet then the equal time correlation function must be odd in parity $F(\mathbf{r}_1, t; \mathbf{r}_2, t) = -F(\mathbf{r}_2, t; \mathbf{r}_1, t)$. However, spin triplet pairs can be even in parity and spin singlet pairs can be odd in parity if the pairing amplitude is odd in time or, equivalently, Matsubara frequency, as was originally proposed for superfluid He^3 [123] and later for superconductivity [124]. This ensures that equal time correlations vanish enforcing the Pauli principle and leads to a rich variety of pairing symmetries. Odd-frequency pairing has been, theoretically, shown to develop in ferromagnetic insulator/superconductor (FMI|SC) [125], ferromagnetic metal/superconductor (FMM|SC) [126], and normal metal/superconductor (N|SC) junctions [127–130]. Several of these works [125, 126, 128, 129] obtained the proximity-induced odd-frequency pairing amplitudes by including the effect of a *spin-active* interface, i.e. an interface that induces a spin dependence of the transmission and reflection amplitudes of the fermionic quasiparticles. These works found that a spin-active interface can modify qualitatively the nature of the pairing amplitude in N|SC, FMI|SC, and FMM|SC heterostructures.

In this work we investigate the effect of a spin-active interface on the symmetry of the superconducting pairing induced in the TI surface by proximity to an s-wave superconductor. Previous works on TI|SC heterostructures [114–117] had not taken into account the presence of a spin-active interface. In principle any interface between two materials whose quasiparticle spin states are different can be thought of as spin-active. However, one could also engineer an interface, A|B, to be spin-active by inserting a thin layer of magnetic material between A and B. Below we develop a model to describe a generic spin-active

interface between two effectively 2D systems. We then apply it to the case of a TI|SC heterostructure with a spin-active interface. Our results show that the presence of a spin-active interface profoundly affects the nature of the proximity-induced superconducting pairing in the TI. In particular, we find that in TI|SC heterostructures with a spin-active interface the odd-frequency components of the pairing amplitude have different spin and spatial structure from the ones of TI|SC heterostructures with no spin-active interface and from the ones of N|SC, FMI|SC, and FMM|SC heterostructures with spin-active interfaces [125-130].

5.1 Model and Setup

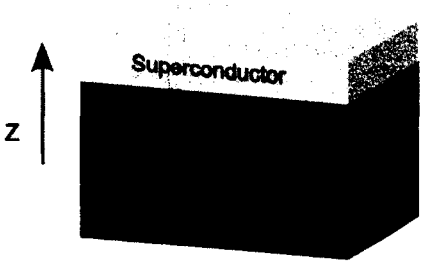

FIG. 5.1: Schematic of topological insulator-superconductor heterostructure. Sketch of the TI|SC heterostructure considered.spin-active interface is present between the superconductor and the 3D topological insulator. The spin-active interface could be realized by a thin layer of magnetic material such as EuO.

Figure 5.1 shows schematically a TI-SC heterostructure with a spin-active interface. We consider three kinds of spin-active interfaces: those which confer a spin-dependent interfacial phase (SDIP) to quasiparticle states at the interface; those that flip the spins of quasiparticles at the interface; and those that do both. By SDIPs we refer to the process whereby quasiparticle states incident on the interface pick up a spin-dependent phase when transmitted $|\uparrow\rangle_{\mathbf{k}} \rightarrow e^{i\theta_{\uparrow,\mathbf{k}}}|\uparrow\rangle_{\mathbf{k}}$ and $|\downarrow\rangle_{\mathbf{k}} \rightarrow e^{i\theta_{\downarrow,\mathbf{k}}}|\downarrow\rangle_{\mathbf{k}}$. The spin and $\mathbf{k}$-dependence of the

phases $\theta_{\alpha,\mathbf{k}}$ are determined by the microscopic details of the interface [129, 131–133]. This process is thought to be a common feature of spin-active interfaces [125, 132, 134–137] and can be thought of as a precession of the incident electron's spin about the magnetization axis of the interface. Let $\eta_{\mathbf{k}} \equiv (\theta_{\uparrow,\mathbf{k}} + \theta_{\downarrow,\mathbf{k}} + \theta_{\uparrow,-\mathbf{k}} + \theta_{\downarrow,-\mathbf{k}})/2$, $\delta\theta_{\mathbf{k}} \equiv \theta_{\uparrow,\mathbf{k}} - \theta_{\downarrow,\mathbf{k}}$ and $\zeta_{\mathbf{k}} \equiv (\delta\theta_{\mathbf{k}} - \delta\theta_{-\mathbf{k}})/2$, using this convention a spin-singlet pair $|\uparrow\rangle_{\mathbf{k}}|\downarrow\rangle_{-\mathbf{k}} - |\downarrow\rangle_{\mathbf{k}}|\uparrow\rangle_{-\mathbf{k}}$ is converted to $e^{i\eta_{\mathbf{k}}}\left(e^{i\zeta_{\mathbf{k}}}|\uparrow\rangle_{\mathbf{k}}|\downarrow\rangle_{-\mathbf{k}} - e^{-i\zeta_{\mathbf{k}}}|\downarrow\rangle_{\mathbf{k}}|\uparrow\rangle_{-\mathbf{k}}\right)$ upon scattering at the interface. Hence a singlet pair in the superconductor develops a triplet component proportional to $\sin\zeta_{\mathbf{k}}$ at the interface. Thus we can see that the most important consequence of the presence of SDIPs is the conversion of purely spin singlet pairing amplitudes to a linear combination of singlet and triplet amplitudes at the interface. Any material that possesses this property could be used to capture the effects we derive for SDIPs. By spin-flipping (SF) we refer to tunneling processes that do not conserve the spin of transmitted electrons. This process could be realized by any material whose quasiparticle states are in a spin state that is a different linear combination of spin up and spin down from the superconductor. An example of this kind of material would be a ferromagnetic half-metal.

The main difference between a topological insulator and other materials for which the effect of spin-active interfaces have been studied is that, at low energies, topological insulator states possess a spin lying in the plane of the surface whose direction is locked with the direction of the momentum. We will show that this affects the symmetries of the induced pairing, creating odd-frequency m = 1 triplet (S = 1; m = 1) correlations for any spin-active interface that confers SDIPs.

To model the system in Fig 5.1 we employ the Hamiltonian: $H = H_{TI} + H_{SC} + H_t$

where:

$$
\begin{aligned}
H_{TI} &= \sum_{\mathbf{k},\lambda,\lambda'} (\hbar v \hat{z} \cdot \boldsymbol{\sigma} \times \mathbf{k} - \mu\sigma_0)_{\lambda\lambda'} c^{\dagger}_{\mathbf{k},\lambda} c_{\mathbf{k},\lambda'} \\
H_{SC} &= \sum_{\mathbf{k},\lambda,\lambda'} \left(\epsilon_{\mathbf{k}} d^{\dagger}_{\mathbf{k},\lambda} d_{\mathbf{k},\lambda} + \hat{\Delta}_{\lambda\lambda'} d^{\dagger}_{\mathbf{k},\lambda} d^{\dagger}_{-\mathbf{k},\lambda'} \right) + \text{h.c.} \\
H_{t} &= \sum_{\mathbf{k},\lambda,\lambda'} \hat{T}_{\lambda\lambda'} c^{\dagger}_{\mathbf{k},\lambda} d_{\mathbf{k},\lambda'} + \text{h.c.}
\end{aligned}
\tag{5.1}
$$

where σ_0 is the 2×2 identity matrix in spin space, $\boldsymbol{\sigma}$ is the vector $(\sigma_1, \sigma_2, \sigma_3)$ formed by 2×2 Pauli matrices in spin space, $\mathbf{k} = (k_x, k_y, 0)$, v is the Fermi velocity of the surface states in the TI, μ is the chemical potential in the TI surface, $c^{\dagger}_{\mathbf{k},\lambda}$ $\left(d^{\dagger}_{\mathbf{k},\lambda}\right)$ creates a quasiparticle with momentum $\mathbf{k}$ and spin λ in the TI surface (superconductor), $\epsilon_{\mathbf{k}}$ is the energy of a superconductor quasiparticle state measured from the chemical potential in the superconductor, $\hat{\Delta} = -\Delta_0 i\sigma_2$ is the order parameter of the superconducting condensate, and $\hat{T} = (t_0\sigma_0 + \mathbf{t} \cdot \boldsymbol{\sigma})$ with $\mathbf{t} = (t_1, t_2, t_3)$. Notice that the tunneling term accounts for the possibility of spin-flip processes at the interface if $\mathbf{t} \neq 0$.

5.2 Proximity-Induced Pairing

To investigate the effect of the spin-active interface on proximity-induced pairing in the TI we calculate the pairing amplitude in the TI as a function of momentum $\mathbf{k}$ and Matsubara frequency ω, $\hat{F}^{TI}(\mathbf{k}, \omega)$. To leading order in $\hat{T}$ we have:

$$
\hat{F}^{TI}(\mathbf{k}, \omega) = \hat{G}^{TI}_0(\mathbf{k}, \omega) \hat{T} \hat{F}^{SC}_{\theta_{\mathbf{k}}}(\mathbf{k}, \omega) \hat{T}^{\mathrm{T}} \hat{G}^{TI}_0(-\mathbf{k}, -\omega)^{\mathrm{T}} \tag{5.2}
$$

where we have included SDIP by a transformation in spin-space at the interface $\hat{F}^{SC}_{\theta_{\mathbf{k}}}(\mathbf{k}, \omega) = e^{i\eta_{\mathbf{k}}} e^{i\frac{\delta\theta_{\mathbf{k}}}{2}\sigma_3} \hat{F}^{SC}_0(\mathbf{k}, \omega) e^{i\frac{\delta\theta_{-\mathbf{k}}}{2}\sigma_3}$, where $\hat{F}^{SC}_0(\mathbf{k}, \omega) = -\hat{\Delta} / \left(\omega^2 + \epsilon^2_{\mathbf{k}} + \Delta^2_0\right)$ is the pairing amplitude in the SC.

Evaluating the expression on the right hand side of Eq (5.2) we find $\hat{F}^{TI}(\mathbf{k}, \omega) =$

$\frac{-i\Delta_0}{(\omega^2+\epsilon_{\mathbf{k}}^2+\Delta_0^2)[(i\omega+\mu)^2-\hbar^2v^2k^2][(i\omega-\mu)^2-\hbar^2v^2k^2]}e^{i\eta_{\mathbf{k}}}\hat{f}^{TI}(\mathbf{k},\omega)$ where

$$\hat{f}^{TI}(\mathbf{k},\omega) = f_0^{TI}\sigma_0 + f_1^{TI}\sigma_1 + f_2^{TI}\sigma_2 + f_3^{TI}\sigma_3 \tag{5.3}$$

and

$$\begin{aligned}
f_0^{TI} &= 2\sin\zeta_{\mathbf{k}}\left[-\left(\omega^2+\mu^2+\hbar^2v^2(k_x^2-k_y^2)\right)(t_0t_1-it_2t_3)\right] \\
&\quad + 2\sin\zeta_{\mathbf{k}}\left[-2\hbar^2v^2k_xk_y\,(t_0t_2+it_1t_3) + i\omega\hbar vk_y(t_0^2-2t_3^2+|\mathbf{t}|^2)\right] \\
&\quad + 2\cos\zeta_{\mathbf{k}}\left[\hbar vk_x\mu(t_0^2-|\mathbf{t}|^2)\right] \\
f_1^{TI} &= -\sin\zeta_{\mathbf{k}}\left[\left(\omega^2+\mu^2-\hbar^2v^2k^2\right)\left(t_0^2-2t_3^2+|\mathbf{t}|^2\right)\right] \\
&\quad - \sin\zeta_{\mathbf{k}}\left[4i\omega\hbar v\left[k_x(t_0t_2+it_1t_3)-k_y(t_0t_1-it_2t_3)\right]\right] \\
f_2^{TI} &= \sin\zeta_{\mathbf{k}}\left[4\mu\hbar v\left[k_x(t_0t_1-it_2t_3)+k_y(t_0t_2+it_1t_3)\right]\right] \\
&\quad - \cos\zeta_{\mathbf{k}}\left[\left(\omega^2+\mu^2+\hbar^2v^2k^2\right)\left(t_0^2-|\mathbf{t}|^2\right)\right] \\
f_3^{TI} &= -2\sin\zeta_{\mathbf{k}}\left[\left(\omega^2+\mu^2-\hbar^2v^2(k_x^2-k_y^2)\right)(t_1t_3-it_0t_2)\right] \\
&\quad - 2\sin\zeta_{\mathbf{k}}\left[-2\hbar^2v^2k_xk_y\,(t_2t_3+it_0t_1) + \omega\hbar vk_x(t_0^2-2t_3^2+|\mathbf{t}|^2)\right] \\
&\quad - 2\cos\zeta_{\mathbf{k}}\left[i\hbar vk_y\mu(t_0^2-|\mathbf{t}|^2)\right].
\end{aligned} \tag{5.4}$$

The $S=1$ $m=\pm1$ components of the pairing amplitude are given by $f_0^{TI}\pm f_3^{TI}$, the $m=0$ triplet component by f_1^{TI}, while the singlet ($S=0$) is given by f_2^{TI}. From Eq (5.4) we can see that the presence of a spin-active interface induces odd-frequency triplet correlations in the TI, similar to the case where the TI layer is replaced by a 3D normal metal or ferromagnetic material [126, 128, 129, 132, 135, 137, 138]. It is interesting to note that the $m=\pm1$ amplitudes possess a non-trivial $\mathbf{k}$-dependence reminiscent of a chiral state. Specifically, the odd-frequency components are proportional to $|\mathbf{k}|\sin\zeta_{\mathbf{k}}e^{\mp i\phi_{\mathbf{k}}}$ while the even-frequency components are proportional to $|\mathbf{k}|^2\sin\zeta_{\mathbf{k}}e^{\mp i2\phi_{\mathbf{k}}}$ where $\phi_{\mathbf{k}}=\tan^{-1}k_y/k_x$. From Eqs (5.4) we note that if there are no SDIPs, that is $\zeta_{\mathbf{k}}=0$, then the f_1^{TI} component

does not contribute to $\hat{f}^{TI}(\mathbf{k},\omega)$ and the f_0^{TI} and f_3^{TI} components are proportional to μ so that at the Dirac point no triplet correlations are induced in the TI at this order. The next term contributing to $\hat{F}^{TI}(\mathbf{k},\omega)$ is proportional to $\hat{T}^4$ and at this order we do find odd-frequency triplet correlations even with $\zeta_{\mathbf{k}} = 0$, however these amplitudes are orders of magnitude smaller than the singlet contribution in Eq (5.4) and will not be presented here.

If instead we have $\zeta_{\mathbf{k}} \neq 0$ and no spin-flipping ($\mathbf{t} = 0$) then Eqs (5.4) simplify to:

$$\begin{aligned} f_0^{TI} &= 2t_0^2\hbar v\left[\mu\cos\zeta_{\mathbf{k}}k_x + i\omega\sin\zeta_{\mathbf{k}}k_y\right] \\ f_1^{TI} &= -t_0^2\sin\zeta_{\mathbf{k}}\left(\omega^2+\mu^2-\hbar^2v^2k^2\right) \\ f_2^{TI} &= -t_0^2\cos\zeta_{\mathbf{k}}\left(\omega^2+\mu^2+\hbar^2v^2k^2\right) \\ f_3^{TI} &= -2t_0^2\hbar v\left[\omega\sin\zeta_{\mathbf{k}}k_x + i\mu\cos\zeta_{\mathbf{k}}k_y\right]. \end{aligned} \tag{5.5}$$

From these equations we see that even in the absence of spin-flip processes SDIPs lead to chiral odd-frequency $m = \pm 1$ triplet pairing on a TI surface. However, spin-flip processes are necessary to give rise to odd-frequency $m = 0$ triplet pairing and even-frequency $m = \pm 1$ triplet pairing at the Dirac point of the TI.

To gain some insight, we compare these results to the case of a X|S junction with a spin-active interface where we take X to be a 2D material described by the Hamiltonian $H_X = \sum_{\mathbf{k},\lambda}(\xi_{\mathbf{k}}\sigma_0 + \mathbf{h}\cdot\boldsymbol{\sigma})_{\lambda\lambda}a^\dagger_{\mathbf{k},\lambda}a_{\mathbf{k},\lambda}$ where we assume $\xi_{-\mathbf{k}} = \xi_{\mathbf{k}}$. For $\mathbf{h} = 0$ this describes a 2D normal metal (X=N), for $\mathbf{h} \neq 0$ this describes a ferromagnet (X=F). We make a distinction between two limits of the F case, one in which $\mathbf{h} = (0,0,h)$ (FZ) and an easy-plane ferromagnet $\mathbf{h} = h(\cos\phi, \sin\phi, 0)$ (FE). To calculate the leading order contribution to the anomalous Green's function for this kind of system, $\hat{F}^X(\mathbf{k},\omega)$, (ignoring the effect of the exchange field on the superconductor) we replace $\hat{G}_0^{TI}(\mathbf{k},\omega)$ in Eq (5.2) with $\hat{G}_0^X(\mathbf{k},\omega) = \frac{1}{(\xi_{\mathbf{k}}-i\omega)^2-|\mathbf{h}|^2}[(i\omega-\xi_{\mathbf{k}})\sigma_0 + \mathbf{h}\cdot\boldsymbol{\sigma}]$. Evaluating the resulting expression we find $\hat{F}^X(\mathbf{k},\omega) =$

$\frac{-i\Delta_0}{(\omega^2+\Delta^2+\epsilon_{\mathbf{k}}^2)[\xi_{\mathbf{k}}^4+2\xi_{\mathbf{k}}^2(\omega^2-|\mathbf{h}|^2)+(\omega^2+|\mathbf{h}|^2)^2]} e^{i\eta_{\mathbf{k}}} \hat{f}^X(\mathbf{k},\omega)$ where

$$\hat{f}^X(\mathbf{k},\omega) = f_0^X\sigma_0 + f_1^X\sigma_1 + f_2^X\sigma_2 + f_3^X\sigma_3. \tag{5.6}$$

and

$$\begin{aligned}
f_0^X &= -i2\cos\zeta_{\mathbf{k}}\omega h_2\left(t_0^2 - |\mathbf{t}|^2\right) \\
&\quad - 2\sin\zeta_{\mathbf{k}}\left(h_1\xi_{\mathbf{k}} + ih_2h_3\right)\left(t_0^2 - 2t_3^2 + |\mathbf{t}|^2\right) \\
&\quad + 2\sin\zeta_{\mathbf{k}}\left(\omega^2 + \xi_{\mathbf{k}}^2 - 2h_2^2 + |\mathbf{h}|^2\right)\left(t_0t_1 - it_2t_3\right) \\
&\quad + 4\sin\zeta_{\mathbf{k}}\left(h_1h_2 + ih_3\xi_{\mathbf{k}}\right)\left(t_0t_2 + it_1t_3\right) \\
f_1^X &= 2\cos\zeta_{\mathbf{k}}\omega h_3\left(t_0^2 - |\mathbf{t}|^2\right) \\
&\quad - \sin\zeta_{\mathbf{k}}\left(\omega^2 + \xi_{\mathbf{k}}^2 + 2h_1^2 - |\mathbf{h}|^2\right)\left(t_0^2 - 2t_3^2 + |\mathbf{t}|^2\right) \\
&\quad - 4\sin\zeta_{\mathbf{k}}\left(h_2h_3 + ih_1\xi_{\mathbf{k}}\right)\left(t_2t_3 + it_0t_1\right) \\
&\quad + 4\sin\zeta_{\mathbf{k}}\left(h_2\xi_{\mathbf{k}} + ih_1h_3\right)\left(t_0t_2 + it_1t_3\right) \\
f_2^X &= \cos\zeta_{\mathbf{k}}\left(\omega^2 + \xi_{\mathbf{k}}^2 - |\mathbf{h}|^2\right)\left(t_0^2 - |\mathbf{t}|^2\right) \\
&\quad - 2\sin\zeta_{\mathbf{k}}\omega\left[2h_1\left(t_1t_3 - it_0t_2\right) + 2h_2\left(t_2t_3 + it_0t_1\right)\right] \\
&\quad + 2\sin\zeta_{\mathbf{k}}\omega h_3\left(t_0^2 - 2t_3^2 + |\mathbf{t}|^2\right) \\
f_3^X &= 2\cos\zeta_{\mathbf{k}}\omega h_1\left(t_0^2 - |\mathbf{t}|^2\right) \\
&\quad + 2\sin\zeta_{\mathbf{k}}\left(h_1h_3 + ih_2\xi_{\mathbf{k}}\right)\left(t_0^2 - 2t_3^2 + |\mathbf{t}|^2\right) \\
&\quad + 2\sin\zeta_{\mathbf{k}}\left(\omega^2 + \xi_{\mathbf{k}}^2 - 2h_1^2 + |\mathbf{h}|^2\right)\left(t_1t_3 - it_0t_2\right) \\
&\quad - 4\sin\zeta_{\mathbf{k}}\left(h_3\xi_{\mathbf{k}} + ih_1h_2\right)\left(t_0t_1 - it_2t_3\right).
\end{aligned} \tag{5.7}$$

Notice that the odd-frequency $m = 0$ triplet component is proportional to $h_3\cos\zeta_{\mathbf{k}}$, while the $m = \pm 1$ triplet component is proportional to $(h_2 \pm ih_1)\cos\zeta_{\mathbf{k}}$ hence if the material has a non-zero exchange field then even for $\zeta_{\mathbf{k}} = 0$ there is an odd-frequency

triplet amplitude in contrast to the case of either a normal metal or a TI. At this point we can use the components in Eqs (5.4, 5.7) to explore the properties of the cases noted above. The symmetries for the four systems TI|SC, N|SC, FZ|SC, and FE|SC are summarized in Table 5.1.

TABLE 5.1: Comparison of Proximity-Induced Pairing in TI|SC, N|SC, FZ|SC, and FE|SC

	Interface	TI|SC	N|SC	FZ|SC	FE|SC
Even-ω	No SF or SDIP	$S=0,1;\ m=\pm1$	$S=0$	$S=0$	$S=0$
	SDIP	$S=0,1;\ m=0,\pm1$	$S=0,1;\ m=0$	$S=0,1;\ m=0$	$S=0,1;\ m=0,\pm1$
	SF	$S=0,1;\ m=\pm1$	$S=0$	$S=0$	$S=0$
	SF and SDIP	$S=0,1;\ m=0,\pm1$	$S=0,1;\ m=0,\pm1$	$S=0,1;\ m=0,\pm1$	$S=0,1;\ m=0,\pm1$
Odd-ω	No SF or SDIP			$S=1;\ m=0$	$S=1;\ m=\pm1$
	SDIP	$S=1;\ m=\pm1$		$S=0,1;\ m=0$	$S=1;\ m=\pm1$
	SF			$S=1;\ m=0$	$S=1;\ m=\pm1$
	SF and SDIP	$S=1;\ m=0,\pm1$		$S=0,1;\ m=0$	$S=0,1;\ m=\pm1$

Table 5.1 shows that the presence of an interface with SDIPs induces odd-frequency triplet correlations in TI|SC heterostructures. Another feature of Table 5.1 is that the FZ|SC and N|SC only develop $m = \pm1$ triplet amplitudes if the interface both confers SDIPs and is spin-flipping, in contrast to the TI|SC and FE|SC which exhibit $m = \pm1$ triplet amplitudes for all four interfaces. This can be explained by realizing that the SDIPs convert a singlet pair into a linear combination of singlet and m = 0 triplet but this mechanism cannot align two spins in a Cooper pair that were originally anti-aligned. Spin-flipping processes can take the $m = 0$ triplet state and rotate it out of the plane to produce an $m = \pm1$ triplet. In the case of the FE and TI, the spin of the eigenstates for these materials lies in the x-y plane and hence these states are already a linear combination of $|\uparrow\rangle$ and $|\downarrow\rangle$. This acts as an intrinsic mechanism for aligning the spins of the paired quasiparticles. For this reason we can see that the FE and TI exhibit $m = \pm1$ triplet contributions for all four interfaces.

It is worth noting that the symmetries of the induced pairings in the FE are not sensitive to the value of the chemical potential while in the case of the TI, for interfaces that lack SDIPs, the only triplet contributions are proportional to μ so that at the Dirac point an interface without SDIPs will only give rise to singlet pairing in the TI. Another difference between the TI and FE is that for the TI odd-frequency pairing only develops in the presence of SDIPs while odd-frequency pairing is ubiquitous in the FE (and FZ) for all four interfaces. These qualitative differences between the TI and FE results can be attributed to the chiral spin structure of the TI, i.e. the fact that $\mathbf{k} \to -\mathbf{k}$ implies $\mathbf{s} \to -\mathbf{s}$, where $\mathbf{s}$ is the spin of an electron on the surface of a TI.

Note that for the normal metal we see that no odd-frequency amplitudes are induced at this order. We attribute this to the trivial spin structure of the normal metal whose Green's function is even in frequency and proportional to the identity in spin space so the only way to induce odd-frequency correlations in this material would be through processes of higher order in $\hat{T}$.

5.3 Summary

In this chapter we analyzed proximity-induced superconductivity in TI|S heterostructures with a spin-active interface. We found the proximity-induced pairing amplitudes in the TI to be qualitatively different from non-chiral materials. The presence of spin-dependent interfacial phases give rise to odd-frequency $m = \pm 1$ triplet correlations. This appears to be due to the unique spin structure of the TI surface states. Another interesting feature of the $m = \pm 1$ triplet correlations for TI|S structures with a spin active interface is the fact that both the even and odd-frequency contributions possess non-trivial $\mathbf{k}$-dependence reminiscent of a chiral state, the odd-frequency terms being proportional to $\sin\zeta_{\mathbf{k}} e^{-i\phi_{\mathbf{k}}}$ and the even-frequency terms being proportional to $\sin\zeta_{\mathbf{k}} e^{-i2\phi_{\mathbf{k}}}$. Additionally,

we found the magnitude of the odd-frequency pairing amplitude to be dependent on the direction of $\mathbf{t}$ a quantity that could be tuned by appropriately manufacturing the interface. Depending on the degree of control one has on the direction of $\mathbf{t}$, this could allow for the ability to turn the odd-frequency pairing amplitude on or off as desired.

CHAPTER 6

Many-body instabilities and mass generation in slow Dirac materials

This chapter is based on work discussed in [139]. One important way the Dirac nature of quasiparticles manifests itself is in the effect of interactions. If the quasiparticles of a system obey the Schrödinger equation then the ratio of the average interparticle Coulomb energy to the average kinetic energy, $r_s = E_C/E_K$, is related to the density by $r_s \propto n^{-1/d}$, [18, 140] where the constant of proportionality depends on characteristics of the material. In contrast to normal metals, for Dirac materials this ratio is a characteristic of the system, independent of the electron density, given by $\alpha \equiv E_C/E_K = e^2/(\hbar\epsilon v)$. In this expression e is the charge of the electron, ϵ is the material's dielectric constant, $\hbar$ is the reduced Planck constant, and v is the speed of the Dirac particles. Much work has gone into the study of the phase diagram of graphene with respect to the strength of Coulomb interactions [4, 18, 140–146]. Some theoretical studies indicate the possibile existence of a critical value of the coupling constant, α_c, such that if $\alpha < \alpha_c$ the spectrum remains gapless and if $\alpha > \alpha_c$ the system flows toward the strong coupling regime and is likely to develop a

gap [18]. Thus far, perturbative and numerical results suggest a theoretical critical value of $\alpha_c \approx 1$ [18, 143] while experiments involving suspended graphene, for which $\alpha \approx 2.2$, indicate that no gap exists larger than 0.1meV [147]. Therefore, it is safe to say that the ground state of Dirac materials in the strong coupling regime is not currently understood. For this reason we propose to study a class of materials with much smaller Fermi velocity than that of graphene since this class of materials is likely to possess $\alpha \gg \alpha_c$ and would be a better candidate for experiments probing the strong coupling regime in Dirac materials.

In previous chapters we have discussed some of the experimentally verified examples of three-dimensional (3D) topological insulators (TIs) which include: Bi_2Se_3, Bi_2Te_3, and Sb_2Te_3, all of which have Fermi velocities roughly half of that in graphene [66, 148]. However, there is another class of topological insulators, the topological Kondo insulators (TKI), in which the bulk states are formed by renormalized f-electron levels which hybridize with conduction electrons to form a milivolt-scale gap in the bulk spectrum [149–151]. The small gap in these materials combined with the large bulk effective mass imply that the surface Fermi velocity could be quite small. Some materials theoretically predicted to fall into this category include SmB_6 [152], YbB_{12} [153], and PuB_6 [154]. Furthermore, there is a growing body of experimental evidence demonstrating that SmB_6 does in fact host metallic surface states [155, 156].

In this chapter we present a model to study the surface states of a TKI and proceed to investigate the possible ordered ground states for these systems within a mean field theory. From this analysis, we find regions of parameter space for the model that admit spin density wave and charge density wave solutions. For the case of strictly repulsive interactions we find that these ordered solutions lie within the region of parameter space corresponding to the strong coupling regime of Dirac materials ($\alpha > \alpha_c \approx 1$).

6.1 Theoretical Model and Methods

To model the 2D surface states of a TKI, we consider a Hamiltonian defined on a square lattice:

$$\begin{aligned} H_0 = -i\frac{A}{2}\sum_{\alpha,\beta,\sigma}\sum_{\langle ij\rangle}\psi^{\dagger}_{i,\alpha,\sigma}\hat{z}\cdot\left(\hat{R}_{ij}\times\boldsymbol{\sigma}\right)_{\alpha\beta}\psi_{j,\beta,\sigma} \\ +\sum_{\alpha,\beta,\sigma}\sum_{i,j}\Gamma_{ij}\psi^{\dagger}_{i,\alpha,\sigma}\sigma_{\alpha\beta}\psi_{j,\beta,\sigma} \end{aligned} \tag{6.1}$$

where α and β are orbital indices, σ is a spin index, $\hat{R}_{ij}$ is the unit vector pointing from lattice site j to lattice site i, and the matrix $\hat{\Gamma}$ is defined as

$$\Gamma_{ij} = \begin{cases} 4\Gamma & ;\ i = j \\ -\Gamma & ;\ i,j \text{ nearest neighbors} \\ 0 & ;\ \text{otherwise.} \end{cases} \tag{6.2}$$

The term proportional to A leads to the formation of four separate Dirac points in the Brillouin zone. The term proportional to Γ acts as a momentum-dependent mass term which gaps out all of the Dirac points except the one at $\mathbf{k} = 0$ allowing the model to represent the surface states of a strong TI. Recalling the Nielsen-Ninomiya theorem [36] this may seem too good to be true. In fact, in the process of adding this term we have rendered our Hamiltonian spin degenerate, in a sense trading chirality for a linear energy dispersion. The energy eigenvalues associated with this Hamiltonian in k-space are given by:

$$\begin{aligned} E^{\pm}_{\mathbf{k}} = \pm 4\Gamma\left[\sin^2\frac{ak_x}{2}+\sin^2\frac{ak_y}{2}\right] \\ \times\sqrt{1+\left(\frac{A}{4\Gamma}\right)^2\frac{\sin^2 ak_x+\sin^2 ak_y}{\left[\sin^2\frac{ak_x}{2}+\sin^2\frac{ak_y}{2}\right]^2}}. \end{aligned} \tag{6.3}$$

Expanding this dispersion for small k along the k_x direction we find:

$$E_k^{\pm} \approx \pm \left(aAk + \frac{(3\Gamma^2 - A^2)a^3}{6A} k^3 \right). \tag{6.4}$$

Thus, we can see that to first order in k the dispersion matches the Dirac dispersion with Fermi velocity given by $aA/\hbar$. In Fig. 6.1 we plot the full dispersion from Eq. (6.3) for different ranges of k to demonstrate the Dirac dispersion for a few different values of the Fermi velocity. It shows that near the Dirac point the parameter A controls the Fermi velocity; however, for $A \ll \Gamma$ we can see that the cubic term in Eq. (6.4) begins to dominate and the dispersion away from the Dirac point becomes noticeably less linear. Since we are most interested in the regime in which the model best describes a Dirac material, in this work we focus on the case in which the chemical potential is close to the Dirac point.

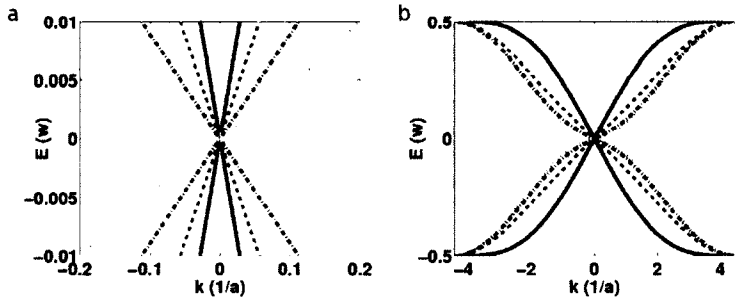

FIG. 6.1: Band structure for model of topological Kondo insulator. Plots of the band structure given by Eq. (6.3) along the diagonal of the square Brillouin zone using four different values of the parameter A: {1/4 (solid, black), 1/8 (dashed, red), 1/16 (dashed-dot, blue), and 1/32 (dotted, green)}; in two different momentum ranges: (a) from $\mathbf{k} = (-1/5a, -1/5a)$ to $\mathbf{k} = (1/5a, 1/5a)$ and (b) from $\mathbf{k} = (-\pi/a, -\pi/a)$ to $\mathbf{k} = (\pi/a, \pi/a)$. All energies are in units of the bandwidth.

In terms of the model parameters the bandwidth is given by:

$$w = \begin{cases} 16\Gamma & ; \ A \leq 4\Gamma \\ \dfrac{4A^2}{\sqrt{2A^2 + 16\Gamma^2}} & ; \ A > 4\Gamma \end{cases}$$

Note that for $A \leq 4\Gamma$ the bandwidth is a constant set by the model parameter Γ. In the analysis that follows we restrict the range of A to $A \leq 4\Gamma$ and present all energies in units of the bandwidth $w = 16\Gamma$. We also present all distances in units of the lattice constant a.

To account for interactions we consider the full Hamiltonian: $H = H_0 + H_I$, where H_I takes on the form:

$$\begin{aligned} H_I = & \frac{V_0}{2} \sum_{\sigma,\sigma'} \sum_{i \neq j} \frac{e^{-|\mathbf{r}_i - \mathbf{r}_j|/\lambda}}{\sqrt{|\ \mathbf{r}_i - \mathbf{r}_j\ |^2 + d^2}} \psi^\dagger_{i,f,\sigma} \psi_{i,f,\sigma} \psi^\dagger_{j,f,\sigma'} \psi_{j,f,\sigma'} \\ & - U \sum_i \psi^\dagger_{i,f,\uparrow} \psi_{i,f,\uparrow} \psi^\dagger_{i,f,\downarrow} \psi_{i,f,\downarrow} \end{aligned} \tag{6.5}$$

where V_0 controls the strength of the long-range Coulomb interaction between f-electrons and U is introduced as an on-site interaction between f-electrons, λ is a screening length, and d is a short distance cutoff.

In our calculations, we replace the exact interaction term H_I with the mean field Hamiltonian:

$$\begin{aligned} H_I^{MF} = & V_0 \sum_{\sigma,\sigma'} \sum_{i \neq j} \frac{e^{-|\mathbf{r}_i - \mathbf{r}_j|/\lambda}}{\sqrt{|\ \mathbf{r}_i - \mathbf{r}_j\ |^2 + d^2}} \langle n_{i,f,\sigma} \rangle \psi^\dagger_{j,f,\sigma'} \psi_{j,f,\sigma'} \\ & - U \sum_i \left(\langle n_{i,f,\uparrow} \rangle \psi^\dagger_{i,f,\downarrow} \psi_{i,f,\downarrow} + \langle n_{i,f,\downarrow} \rangle \psi^\dagger_{i,f,\uparrow} \psi_{i,f,\uparrow} \right) \\ & + \sum_i \left(\Delta_i \psi^\dagger_{i,f,\uparrow} \psi^\dagger_{j,f,\downarrow} + \Delta_i^* \psi_{i,f,\downarrow} \psi_{j,f,\uparrow} \right) + E_0. \end{aligned} \tag{6.6}$$

If we wish to include an attractive on-site interaction between f-electrons we set $U > 0$; however, if we wish to include on-site Coulomb repulsion we can set $U = -V_0/d$. We may

choose to write this in a more compact notation as:

$$H_I^{MF} = \sum_{\alpha,\beta,\sigma,\sigma'} \sum_{i,j} W_{i\alpha\sigma,j\beta\sigma'} \psi^\dagger_{j,\beta,\sigma'} \psi_{j,\beta,\sigma'} + \sum_i \left(\Delta_i \psi^\dagger_{i,f,\uparrow} \psi^\dagger_{j,f,\downarrow} + \Delta_i^* \psi_{i,f,\downarrow} \psi_{j,f,\uparrow} \right) + E_0$$

where

$$W_{i\alpha\sigma,j\beta\sigma'} = \begin{cases} V_0 \frac{e^{-|\mathbf{r}_i - \mathbf{r}_j|/\lambda}}{\sqrt{|\mathbf{r}_i - \mathbf{r}_j|^2 + d^2}} \langle n_{i,f,\sigma} \rangle \delta_{\alpha\beta} \delta_{\alpha f} & ; \ i \neq j \\ -U \langle n_{i,f,\sigma} \rangle \delta_{\alpha\beta} \delta_{\alpha f} (1 - \delta_{\sigma\sigma'}) & ; \ i = j \end{cases}$$

and

$$\Delta_i \equiv U \langle \psi_{i,f,\uparrow} \psi_{j,f,\downarrow} \rangle .$$

Equipped with this mean-field Hamiltonian we perform a Bogoliubov transformation:

$$\psi_{i,\alpha,\uparrow} = \sum_n \left(\gamma_{n\uparrow} u_{i,\alpha,n,\uparrow} - \gamma^\dagger_{n\downarrow} v^*_{i,\alpha,n,\uparrow} \right)$$
$$\psi_{i,\alpha,\downarrow} = \sum_n \left(\gamma_{n\downarrow} u_{i,\alpha,n,\downarrow} + \gamma^\dagger_{n\uparrow} v^*_{i,\alpha,n,\downarrow} \right)$$

where $\gamma^\dagger_{n\sigma}$ ($\gamma_{n\sigma}$) creates (annihilates) an eigenstate of the mean-field Hamiltonian H. It can be shown that the coefficients u and v satisfy the following equations:

$$\begin{aligned} \epsilon_{n,\uparrow} u_{i,\alpha,n,\uparrow} &= \sum_{j,\beta} H_{i\alpha\uparrow,j\beta\uparrow} u_{j,\beta,n,\uparrow} + \Delta_i v_{i,f,n,\downarrow} \\ \epsilon_{n,\uparrow} v_{i,\alpha,n,\downarrow} &= -\sum_{j,\beta} H^*_{i\alpha\downarrow,j\beta\downarrow} v_{j,\beta,n,\downarrow} + \Delta_i^* u_{i,f,n,\uparrow} \\ \epsilon_{n,\downarrow} u_{i,\alpha,n,\downarrow} &= \sum_{j,\beta} H_{i\alpha\downarrow,j\beta\downarrow} u_{j,\beta,n,\downarrow} + \Delta_i v_{i,f,n,\uparrow} \\ \epsilon_{n,\downarrow} v_{i,\alpha,n,\uparrow} &= -\sum_{j,\beta} H^*_{i\alpha\uparrow,j\beta\uparrow} v_{j,\beta,n,\uparrow} + \Delta_i^* u_{i,f,n,\downarrow} \end{aligned} \tag{6.7}$$

where $H_{i\alpha\sigma,j\beta\sigma'} \equiv H^{(0)}_{i\alpha\sigma,j\beta\sigma'} + W_{i\alpha\sigma,j\beta\sigma'}$ and $\epsilon_{n,\sigma}$ are eigenvalues of $H = H_0 + H_I^{MF}$.

Given the solutions to these equations we can write the mean fields as:

$$\begin{aligned}
\langle n_{i,\alpha,\uparrow} \rangle &= \sum_n \mid u_{i,\alpha,n,\uparrow} \mid^2 f(\epsilon_{n,\uparrow}) \\
&\quad + \sum_n \mid v_{i,\alpha,n,\downarrow} \mid^2 (1 - f(\epsilon_{n,\downarrow})) \\
\langle n_{i,\alpha,\downarrow} \rangle &= \sum_n \mid u_{i,\alpha,n,\downarrow} \mid^2 f(\epsilon_{n,\downarrow}) \\
&\quad + \sum_n \mid v_{i,\alpha,n,\uparrow} \mid^2 (1 - f(\epsilon_{n,\uparrow})) \\
\Delta_i &= U \sum_n v^*_{i,f,n,\downarrow} u_{i,f,n,\uparrow} (1 - f(\epsilon_{n,\uparrow})) \\
&\quad - U \sum_n v^*_{i,f,n,\uparrow} u_{i,f,n,\downarrow} f(\epsilon_{n,\downarrow})
\end{aligned} \tag{6.8}$$

where $f(\epsilon) = \frac{1}{e^{\epsilon/k_B T}+1}$ is the the Fermi-Dirac distribution function at temperature T and k_B is the Boltzmann constant. Given an initial set of model parameters and a temperature, Eqs. (6.7) and (6.8) allow us to solve for the density profile and superconducting order parameter, Δ, self-consistently. In the next section we discuss our progress toward solving these equations.

In some cases multiple solutions for the same model parameters may be found. In this case it is useful to compare the free energy associated with each of the solutions, given by: $F = k_B T \ln Z$, where Z is the partition function. The ground state of the system will be given by the solution with the lowest free energy.

6.2 Numerical Results and Discussion

While it is straightforward to numerically solve Eqs. (6.7) and (6.8) for a finite system, we can make the computation more efficient by using the supercell technique

[157], as explained in Appendix A. For a system with a 10×10 real space unitcell and 8×8 supercell we solved for self-consistent solutions to Eqs. (6.7) and (6.8). For the following results we focused on the case of nearest neighbor Coulomb interactions only and the zero temperature limit. In Eq (6.6) we used a screening length of $\lambda = 1$ and a lattice cutoff of $d = 1$. We considered two limiting cases: the case of a repulsive on-site interaction ($U = -V_0$), and the case of an attractive on-site interaction that scales with the Coulomb interaction ($U = V_0$).

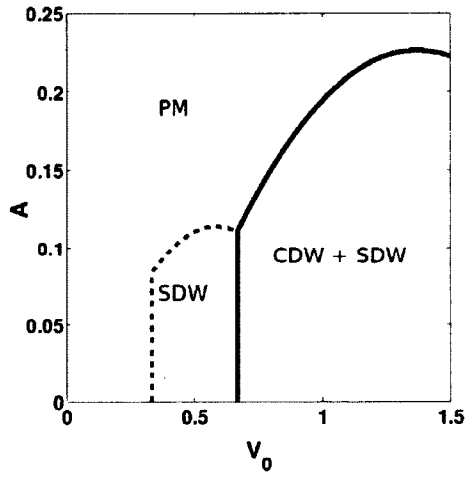

FIG. 6.2: Phase diagram for topological Kondo insulator with repulsive on-site interaction. Plot of the phases for the self-consistent solutions found in different regions of the A,V_0-plane. Note that the region below the line $A = 0.25V_0$ appears to favor the formation of nontrivial order, suggesting a value of α_c of at least 4. The region enclosed by the red dashed line favors the formation of spin density wave order while in the region enclosed by the black solid line we find both spin density wave and charge density wave solutions. Outside of these regions the solution is paramagnetic (PM).

Starting from initial seeds that possessed antiferromagnetic, ferromagnetic, checkerboard and stripe charge density wave (CDW) order in addition to random seeds we found self-consistent solutions for Eqs. (6.7) and (6.8) using a convergence criterion of 10^{-3}. Some of the self-consistent solutions that emerged from the different seeds for the same model parameters differed from each other. In these cases the one with the lowest free

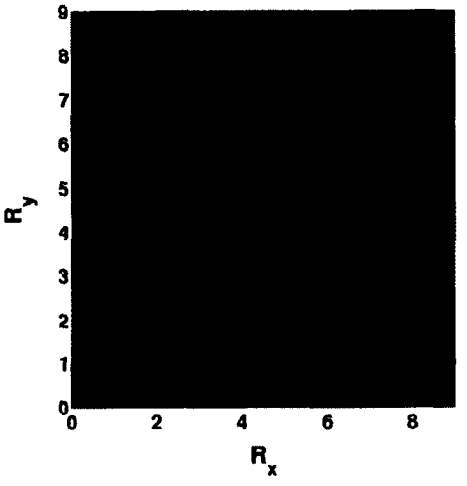

FIG. 6.3: Charge density wave solution. Plot of the density modulations over a 10×10 real space unit cell, as observed in the SDW and CDW regions shown in Fig.s 6.2 and 6.4.

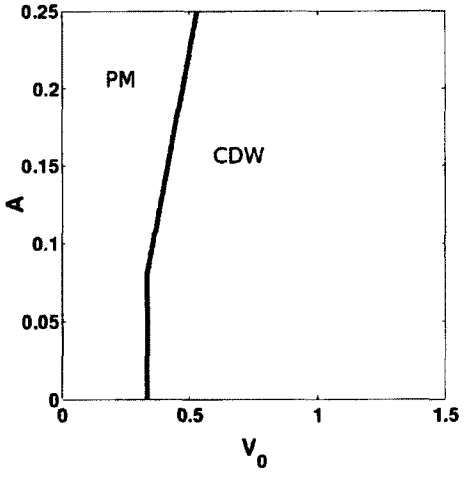

FIG. 6.4: Phase diagram for topological Kondo insulator with attractive on-site interaction. Plot of the phases for the self-consistent solutions found in different regions of the A,V_0-plane for attractive on-site interaction. In the the region to the right of the solid black line the self-consistent solutions possessed charge density wave order, outside of this region the solution was paramagnetic (PM).

energy was taken to be the solution. In Fig. 6.2 we show the regions of parameter space for which we found solutions in the case of repulsive on-site interactions while in Fig. 6.4 we show the regions of parameter space for which we found solutions in the case with attractive on-site interactions.

First, we consider the case of on-site repulsion, ($U = -V_0$), Fig. (6.2). Note that the general trend is consistent with our expectations for Dirac materials. In the region of strong coupling, $\alpha = V_0/A > \alpha_c$, we find Coulomb-driven ordered states, while in the weak coupling region, $V_0/A < \alpha_c$, a paramagnetic (PM) normal metallic state exists. These results are consistent with a value of α_c as high as 6. Additionally, it appears that there is a critical value of the coupling, $V_c \approx w/3$, for this model below which the solution is trivial. This is in contrast to the case of a Dirac continuum model in which the only parameter governing the Coulomb interaction is α. This difference can be attributed to the fact that for very small values of A the band structure appears less linear and eventually the cubic term becomes more important, as we can see from Eq. (6.4). It is reasonable to expect that real materials which host slow Dirac states will typically have similar behavior since the bands for these materials are expected to develop nonzero curvature away from the Dirac point [150, 151, 155, 156].

Taking a closer look at Figure 6.2 we can see that there are three distinct regions of the V_0,A-plane: a region favoring spin density wave (SDW) order; a region in which SDW and CDW coexist; and a region in which the solution was PM. Both SDW and CDW modulations exhibited a checkerboard pattern as shown in the sample plot in Fig 6.3. Intermediate states were also observed but these appear to be higher energy excitations. In the SDW region the boundary for the phase along the V_0 axis, at approximately one third of the bandwidth, defines the critical coupling, V_c. We find that above another critical value of V_0 CDW order begins to coexist with the SDW. In the coexistence region for some model parameters we were able to find solutions with exclusively CDW order but

it is unclear whether these solutions indicated the existence of an additional region of the plane in which CDW is truly favored over SDW order, further calculations will be needed to answer this question.

Next we turn our attention to the case in which we include an on-site attraction, ($U = V_0$), as shown in Fig. 6.4. In this case we find two regions: a region with CDW and a PM region. Again, these density modulations followed a checkerboard pattern. The region that favors CDW begins at $V_0 \approx w/3$ and covers the rest of the plane. It is interesting to note that the CDW order appears for $V_0 > w/3$ which is the same as V_c for the case with repulsive on-site interactions. The region of the plane exhibiting CDW order is consistent with $\alpha_c \approx 1$. It should be noted that some of the self-consistent solutions we found near the transition region $V_0 \approx w/3$ seemed to possess a small superconducting order parameter; however, this order parameter was usually just below the convergence criterion (even when the convergence criterion was lowered to 10^{-7}). We attribute the absence of a superconducting region to the fact that we restricted ourselves to the case of half-filling in which there was no density of states to allow for superconducting pairing. A more detailed study of the region near $V_0 \approx w/3$ may be interesting for future work studying this model away from half-filling.

Note from Figure 6.4 the absence of any regions with magnetic order, in contrast to Figure 6.2 in which SDW order was found. This can be accounted for by a heuristic argument based on Eq 6.6. Notice that the spin-dependent terms in the mean field Hamiltonian are given by $-U\sum_i \left(\langle n_{i,f,\uparrow}\rangle \psi^\dagger_{i,f,\downarrow}\psi_{i,f,\downarrow} + \langle n_{i,f,\downarrow}\rangle \psi^\dagger_{i,f,\uparrow}\psi_{i,f,\uparrow}\right)$, thus the expectation value of the contribution to the total energy will be $-2U\sum_i \langle n_{i,f,\uparrow}\rangle\langle n_{i,f,\downarrow}\rangle$. For $U > 0$ we can see that the energy can be minimized if the sum $\sum_i \langle n_{i,f,\uparrow}\rangle\langle n_{i,f,\downarrow}\rangle$ takes on its maximum possible value. Each term of this sum has a maximum value when $\langle n_{i,f,\uparrow}\rangle = \langle n_{i,f,\downarrow}\rangle = 1/2$. Therefore the minimum energy can be expected to be achieved in a state with no magnetic order. However, for $U < 0$ the system can minimize its energy through an on-site spin

polarization.

6.3 Summary

In this chapter we presented a model for studying the surface states of a class of topological Kondo insulators and explored the dependence of the band structure on the model parameters, identifying the parameters which determine the Fermi velocity at the Dirac point. We then added interactions to this model, accounting for both Coulomb interactions as well as the possibility of an on-site attractive interaction. Using mean-field theory, at zero temperature, we found self-consistent solutions for different model parameters, investigating the relationship between the Fermi velocity at the Dirac point, the strength of the interactions and the nature of the self-consistent solutions. For the case with on-site repulsion we identified three regions of parameter space with different Fermi velocity and coupling strength: a region which exclusively favored spin density wave order, a region of coexisting spin density wave and charge density wave order, and a paramagnetic normal metallic region. We also identified a critical value of the Coulomb interaction strength $V_c \approx w/3$ below which the solutions were normal metallic. When we considered the case of an attractive on-site interaction we found that the solutions possessed charge density wave order above this same critical Coulomb interaction strength.

CHAPTER 7

Conclusion

In this dissertation we have explored the consequences of the nontrivial interplay between spin and momentum, known as chirality, in various two-dimensional electronic systems. In each system we explored which features were a direct consequence of the unique spin-momentum relation and which were a consequence of the geometry of the band structure.

In Chapter 3 we studied the static and dynamic screening of gapped bilayer graphene using the models discussed in Chapter 2. We found qualitative differences between the dielectric screening function obtained using a simplified 2-band model and that obtained using a more sophisticated 4-band model. In particular we found that, in the presence of a band-gap, the static screening exhibited Kohn anomalies that were absent within the 2-band model. We also found that the plasmon modes had qualitatively different character in the 4-band model compared to 2-band results. Additionally, we studied the effect of trigonal warping on the screening properties of bilayer graphene.

In Chapter 4 we formulated a continuum model to study the low-energy electronic structure of heterostructures formed by graphene on a strong three-dimensional topological

insulator (TI) both for the case of commensurate and incommensurate stacking. We found that the proximity of the TI induced a strong enhancement of the spin-orbit coupling in graphene that can be tuned via the twist angle.

In Chapter 5 we examined the effect of a spin-active interface on the symmetry of proximity-induced superconducting pairing amplitudes in topological insulators. We developed a model to investigate the leading order contribution to the pairing amplitude considering three different kinds of spin-active interfaces: (i) those that induce spin-dependent scattering phases, (ii) those that flip the spin of incident electrons, and (iii) interfaces that both induce spin-dependent phases and flip the spins of incident electrons. We found that in cases (i) and (iii) odd-frequency triplet pairing was induced in the TI while for case (ii) no odd-frequency pairing was induced to leading order. Then, comparing our results to those for normal metals and ferromagnetic materials, we found that the nontrivial spin structure of the TI lead to qualitatively different behavior of the pairing amplitudes.

In Chapter 6 we studied the many-body instabilities of topological Kondo insulators. Using a tight-binding model we identified regions of parameter space in which the system exhibited spin density wave, and charge density wave order. Additionally, we identified a value of the critical coupling for these transitions, highlighting the difference between these results and those obtained using continuum models for Dirac materials.

APPENDIX A

Supercell Technique

The system of equations given by Eqs 6.7 and 6.8 can be solved for finite systems by simple matrix diagonalization. However, the matrix that must be diagonalized is $8N \times 8N$, where N is the number of lattice sites and 8 = 2(spins) × 2(orbitals) × 2(electron-hole). We can see that for 6400 sites this would involve diagonalizing a 51200 × 51200 matrix which is not terribly practical. Using the supercell technique we can decrease the size of the matrix that needs to be diagonalized significantly. In the framework of the supercell technique we recognize that, due to the periodicity of the system, the solutions, $u_{\mathbf{r}_i,\alpha,n,\sigma}$ and $v_{\mathbf{r}_i,\alpha,n,\sigma}$, are Bloch waves. To account for this we write

$$\begin{aligned} u_{\mathbf{r}_i,\alpha,n,\sigma} &= e^{i*\mathbf{r}_i\cdot\mathbf{k}} u_{\mathbf{k},\mathbf{r}_i,\alpha,n,\sigma} \\ v_{\mathbf{r}_i,\alpha,n,\sigma} &= e^{i*\mathbf{r}_i\cdot\mathbf{k}} v_{\mathbf{k},\mathbf{r}_i,\alpha,n,\sigma} \end{aligned} \tag{A.1}$$

where $\mathbf{k}$ is the crystal momentum. After this transformation Eqs 6.7 and 6.8 become:

$$\begin{aligned}
\epsilon_{\mathbf{k},n,\uparrow} u_{\mathbf{k},i,\alpha,n,\uparrow} &= \sum_{j,\beta} H_{i\alpha\uparrow,j\beta\uparrow;\mathbf{k}} u_{\mathbf{k},j,\beta,n,\uparrow} + \Delta_i v_{\mathbf{k},i,f,n,\downarrow} \\
\epsilon_{\mathbf{k},n,\uparrow} v_{\mathbf{k},i,\alpha,n,\downarrow} &= -\sum_{j,\beta} H^*_{i\alpha\downarrow,j\beta\downarrow;\mathbf{k}} v_{\mathbf{k},j,\beta,n,\downarrow} + \Delta^*_i u_{\mathbf{k},i,f,n,\uparrow} \\
\epsilon_{\mathbf{k},n,\downarrow} u_{\mathbf{k},i,\alpha,n,\downarrow} &= \sum_{j,\beta} H_{i\alpha\downarrow,j\beta\downarrow;\mathbf{k}} u_{\mathbf{k},j,\beta,n,\downarrow} + \Delta_i v_{\mathbf{k},i,f,n,\uparrow} \\
\epsilon_{\mathbf{k},n,\downarrow} v_{\mathbf{k},i,\alpha,n,\uparrow} &= -\sum_{j,\beta} H^*_{i\alpha\uparrow,j\beta\uparrow;\mathbf{k}} v_{\mathbf{k},j,\beta,n,\uparrow} + \Delta^*_i u_{\mathbf{k},i,f,n,\downarrow}
\end{aligned} \tag{A.2}$$

and

$$\begin{aligned}
\langle n_{i,\alpha,\uparrow} \rangle &= \frac{1}{M_{xy}} \sum_{n,\mathbf{k}} \mid u_{\mathbf{k},i,\alpha,n,\uparrow} \mid^2 f(\epsilon_{\mathbf{k},n,\uparrow}) \\
&\quad + \frac{1}{M_{xy}} \sum_{n,\mathbf{k}} \mid v_{\mathbf{k},i,\alpha,n,\downarrow} \mid^2 (1 - f(\epsilon_{\mathbf{k},n,\downarrow})) \\
\langle n_{i,\alpha,\downarrow} \rangle &= \frac{1}{M_{xy}} \sum_{n,\mathbf{k}} \mid u_{\mathbf{k},i,\alpha,n,\downarrow} \mid^2 f(\epsilon_{\mathbf{k},n,\downarrow}) \\
&\quad + \frac{1}{M_{xy}} \sum_{n,\mathbf{k}} \mid v_{\mathbf{k},i,\alpha,n,\uparrow} \mid^2 (1 - f(\epsilon_{\mathbf{k},n,\uparrow})) \\
\Delta_i &= \frac{U}{M_{xy}} \sum_{n,\mathbf{k}} v^*_{\mathbf{k},i,f,n,\downarrow} u_{\mathbf{k},i,f,n,\uparrow} (1 - f(\epsilon_{\mathbf{k},n,\uparrow})) \\
&\quad - \frac{U}{M_{xy}} \sum_{n,\mathbf{k}} v^*_{\mathbf{k},i,f,n,\uparrow} u_{\mathbf{k},i,f,n,\downarrow} f(\epsilon_{\mathbf{k},n,\downarrow})
\end{aligned} \tag{A.3}$$

where $\mathbf{k} = \frac{2\pi}{M_{xy}a} \left(\frac{n_x}{N_x}, \frac{n_y}{N_y} \right)$ where $n_x = 1, 2, ..., M_x$ and $n_y = 1, 2, ..., M_y$, M_x and M_y are the number of unitcells in the x and y direction respectively, $M_{xy} = M_x M_y$, N_x and N_y are the number of lattice sites per unitcell in the x and y direction respectively, and we define

$$H_{i\alpha\sigma,j\beta\sigma';\mathbf{k}} \equiv \sum_{\mathbf{R}_j} e^{i\mathbf{k}\cdot(\mathbf{r}_j + \mathbf{R}_j - \mathbf{r}_i)} H_{\mathbf{r}_i\alpha\sigma,(\mathbf{r}_j+\mathbf{R}_j)\beta\sigma'}.$$

Now, a system composed of 6400 sites can be studied by diagonalizing a 10×10 real space system using an 8×8 supercell. This means we only need to diagonalize a 800×800 matrix instead of 51200×51200. Moreover, this diagonalization is performed for each $\mathbf{k}$ independently and thus the procedure may be easily parallelized to further improve performance.

BIBLIOGRAPHY

[1] G. F. Giuliani and G. Vignale, *Quantum theory of the electron liquid* (Cambridge University Press, 2005).

[2] T. Wehling, A. Black-Schaffer, and A. Balatsky, Adv. Phys. **63**, 1 (2014).

[3] O. Vafek and A. Vishwanath, Annual Review of Condensed Matter Physics **5**, 83 (2014).

[4] H. P. Dahal, T. O. Wehling, K. S. Bedell, J.-X. Zhu, and A. Balatsky, Physica B **405**, 2241 (2010).

[5] L. Fu, C. L. Kane, and E. J. Mele, Phys. Rev. Lett. **98**, 106803 (2007).

[6] L. Fu and C. L. Kane, Phys. Rev. B **76**, 045302 (2007).

[7] A. C. Neto, F. Guinea, N. Peres, K. S. Novoselov, and A. K. Geim, Rev. Mod. Phys. **81**, 109 (2009).

[8] M. I. Katsnelson, *Graphene: carbon in two dimensions* (Cambridge University Press, 2012).

[9] K. S. Novoselov, A. K. Geim, S. V. Morozov, D. Jiang, Y. Zhang, S. V. Dubonos, I. V. Grigorieva, and A. A. Firsov, Science **306**, 666 (2004).

[10] A. H. C. Neto, F. Guinea, N. M. R. Peres, K. S. Novoselov, and A. K. Geim, Rev. Mod. Phys. **81**, 109 (2009).

[11] S. Das Sarma, S. Adam, E. H. Hwang, and E. Rossi, Rev. Mod. Phys. **83**, 407 (2011).

[12] E. V. Castro, K. S. Novoselov, S. V. Morozov, N. M. R. Peres, J. M. B. L. D. Santos, J. Nilsson, F. Guinea, A. K. Geim, and A. H. C. Neto, Phys. Rev. Lett. **99**, 216802 (2007).

[13] H. Min, B. Sahu, S. K. Banerjee, and A. H. MacDonald, Phys. Rev. B **75** (2007).

[14] J. Oostinga, H. Heersche, X. Liu, A. Morpurgo, and L. Vandersypen, Nature Materials **7**, 151 (2008).

[15] T. Taychatanapat and P. Jarillo-Herrero, Phys. Rev. Lett. **105**, 166601 (2010).

[16] K. Zou and J. Zhu, Phys. Rev. B **82**, 081407 (2010).

[17] J. Yan and M. S. Fuhrer, Nano Letters **10**, 4521 (2010).

[18] V. N. Kotov, B. Uchoa, V. M. Pereira, F. Guinea, and A. C. Neto, Rev. Mod. Phys. **84**, 1067 (2012).

[19] N. Brandt, S. Chudinov, and Y. Ponomarev, *Semimetals: Graphite and its compounds*, Modern problems in condensed matter sciences (North-Holland, 1988), ISBN 9780444870490, URL `http://books.google.com/books?id=VTobAQAAIAAJ`.

[20] V. N. Kotov, B. Uchoa, V. M. Pereira, F. Guinea, and A. H. Castro Neto, Rev. Mod. Phys. **84**, 1067 (2012).

[21] A. H. C. Neto and F. Guinea, Phys. Rev. Lett. **103**, 026804 (2009).

[22] H. Min, J. E. Hill, N. A. Sinitsyn, B. R. Sahu, L. Kleinman, and A. H. MacDonald, Phys. Rev. B **74**, 165310 (2006).

[23] Y. G. Yao, F. Ye, X. L. Qi, S. C. Zhang, and Z. Fang, Phys. Rev. B **75**, 041401 (2007).

[24] M. Gmitra, S. Konschuh, C. Ertler, C. Ambrosch-Draxl, and J. Fabian, Phys. Rev. B **80**, 235431 (2009).

[25] E. I. Rashba, Phys. Rev. B **79**, 161409 (2009).

[26] G. Giovannetti, P. A. Khomyakov, G. Brocks, P. J. Kelly, and J. van den Brink, Phys. Rev. B **76**, 073103 (2007).

[27] B. Hunt, J. D. Sanchez-Yamagishi, A. F. Young, M. Yankowitz, B. J. LeRoy, K. Watanabe, T. Taniguchi, P. Moon, M. Koshino, P. Jarillo-Herrero, et al., Science **340**, 1427 (2013).

[28] E. McCann and V. Fal'ko, Phys. Rev. Lett. **96**, 086805 (2006).

[29] J. Nilsson, A. H. Castro Neto, F. Guinea, and N. M. R. Peres, Phys. Rev. B **78**, 045405 (2008).

[30] M. Z. Hasan and C. L. Kane, Rev. Mod. Phys. **82**, 3045 (2010).

[31] D. X. Qu, Y. S. Hor, J. Xiong, R. J. Cava, and N. P. Ong, Science **329**, 821 (2010).

[32] H. J. Zhang, C. X. Liu, X. L. Qi, X. Dai, Z. Fang, and S. C. Zhang, Nature Phys. **5**, 438 (2009).

[33] C.-X. Liu, X.-L. Qi, H. Zhang, X. Dai, Z. Fang, and S.-C. Zhang, Phys. Rev. B **82**, 045122 (2010).

[34] D. J. Thouless, M. Kohmoto, M. P. Nightingale, and M. den Nijs, Phys. Rev. Lett. **49**, 405 (1982), URL `http://link.aps.org/doi/10.1103/PhysRevLett.49.405`.

[35] C. L. Kane and E. J. Mele, Phys. Rev. Lett. **95**, 146802 (2005).

[36] H. B. Nielsen and M. Ninomiya, Phys. Lett. B **105**, 219 (1981).

[37] D. Hsieh, D. Qian, L. Wray, Y. Xia, Y. S. Hor, R. J. Cava, and M. Z. Hasan, Nature **452**, 970 (2008).

[38] C. Triola and E. Rossi, Phys. Rev. B **86**, 161408 (2012).

[39] A. F. Young, C. R. Dean, I. Meric, S. Sorgenfrei, H. Ren, K. Watanabe, T. Taniguchi, J. Hone, K. L. Shepard, and P. Kim, Phys. Rev. B **85**, 235458 (2012), URL `http://link.aps.org/doi/10.1103/PhysRevB.85.235458`.

[40] C. R. Dean, A. F. Young, I. Meric, C. Lee., L. Wang, S. Sorgenfrei, K. Watanabe, T. Taniguchi, P. Kim, K. L. Shepard, et al., Nature Nanotechnology **5**, 726 (2010).

[41] L. A. Ponomarenko, A. K. Geim, A. A. Zhukov, R. Jalil, S. V. Morozov, K. S. Novoselov, I. V. Grigorieva, E. H. Hill, V. V. Cheianov, V. I. Fal'Ko, et al., Nature Physics **7**, 958 (2011).

[42] R. T. Weitz, M. T. Allen, B. E. Feldman, J. Martin, and A. Yacoby, Science **330**, 812 (2010).

[43] A. S. Mayorov, D. C. Elias, M. Mucha-Kruczynski, R. V. Gorbachev, T. Tudorovskiy, A. Zhukov, S. V. Morozov, M. I. Katsnelson, A. K. Geim, and K. S. Novoselov, Science **333**, 860 (2011).

[44] F. Freitag, J. Trbovic, M. Weiss, and C. Schönenberger, Phys. Rev. Lett. **108**, 076602 (2012).

[45] J. Velasco, L. Jing, W. Bao, Y. Lee, P. Kratz, V. Aji, M. Bockrath, C. N. Lau, C. Varma, R. Stillwell, et al., Nature Nanotechnology **7**, 156 (2012).

[46] H. Min, G. Borghi, M. Polini, and A. H. MacDonald, Phys. Rev. B **77**, 041407 (2008).

[47] C. H. Zhang and Y. N. Joglekar, Phys. Rev. B **77**, 233405 (2008).

[48] O. Vafek and K. Yang, Phys. Rev. B **81**, 041401 (2010).

[49] Y. Lemonik, I. L. Aleiner, C. Toke, and V. I. Fal'ko, Phys. Rev. B **82**, 201408 (2010).

[50] R. Nandkishore and L. Levitov, Phys. Rev. Lett. **104**, 156803 (2010).

[51] R. Nandkishore and L. Levitov, ArXiv e-prints (2010), 1002.1966.

[52] M. Y. Kharitonov and K. B. Efetov, Phys. Rev. B **78**, 241401 (2008).

[53] M. Y. Kharitonov and K. B. Efetov, Semiconductor Science Technology **25**, 034004 (2010).

[54] F. Zhang, H. Min, M. Polini, and A. H. MacDonald, Phys. Rev. B **81**, 041402 (2010).

[55] E. V. Gorbar, V. P. Gusynin, V. A. Miransky, and I. A. Shovkovy, Phys. Rev. B **86**, 125439 (2012), URL http://link.aps.org/doi/10.1103/PhysRevB.86.125439.

[56] X. Wang and T. Chakraborty, Phys. Rev. B **75**, 041404 (2007).

[57] E. H. Hwang and S. D. Sarma, Phys. Rev. Lett. **101**, 156802 (2008).

[58] G. Borghi, M. Polini, R. Asgari, and A. H. MacDonald, Phys. Rev. B **80**, 241402 (2009).

[59] O. V. Gamayun, Phys. Rev. B **84**, 085112 (2011).

[60] S. Yuan, R. Roldán, and M. I. Katsnelson, Phys. Rev. B **84**, 035439 (2011).

[61] R. Sensarma, E. H. Hwang, and S. Das Sarma, Phys. Rev. B **82**, 195428 (2010).

[62] S. Das Sarma and E. H. Hwang, Phys. Rev. Lett. **102**, 206412 (2009).

[63] E. H. Hwang and S. Das Sarma, Phys. Rev. B **80**, 205405 (2009).

[64] H. Min, E. H. Hwang, and S. Das Sarma, Phys. Rev. B **86**, 081402 (2012), URL http://link.aps.org/doi/10.1103/PhysRevB.86.081402.

[65] X.-F. Wang and T. Chakraborty, Phys. Rev. B **81**, 081402 (2010).

[66] J. Zhang, C. Triola, and E. Rossi, Phys. Rev. Lett. **112**, 096802 (2014).

[67] C. Weeks, J. Hu, J. Alicea, M. Franz, and R. Wu, Phys. Rev. X **1**, 021001 (2011), URL http://link.aps.org/doi/10.1103/PhysRevX.1.021001.

[68] H. Jiang, Z. H. Qiao, H. W. Liu, J. R. Shi, and Q. Niu, Phys. Rev. Lett. **109**, 116803 (2012).

[69] W. H. Dang, H. L. Peng, H. Li, P. Wang, and Z. F. Liu, Nano Lett. **10**, 2870 (2010).

[70] C.-L. Song, Y.-L. Wang, Y.-P. Jiang, Y. Zhang, C.-Z. Chang, L. Wang, K. He, X. Chen, J.-F. Jia, Y. Wang, et al., Applied Physics Letters **97**, 143118 (2010).

[71] K. S. Novoselov, D. Jiang, F. Schedin, T. J. Booth, V. V. Khotkevich, S. V. Morozov, and A. K. Geim, Proc. Nat. Acad. Sci. (USA) **102**, 10451 (2005).

[72] S. Kim, J. Nah, I. Jo, D. Shahrjerdi, L. Colombo, Z. Yao, E. Tutuc, and S. K. Banerjee, Applied Physics Letters **94**, 062107 (2009).

[73] S. Kim, I. Jo, J. Nah, Z. Yaoa, S. K. Banerjee, and E. Tutuc, arXiv:1010.2113v1 (2010).

[74] S. Kim and E. Tutuc, Solid State Communications **152**, 1283 (2012).

[75] R. V. Gorbachev, A. K. Geim, M. I. Katsnelson, K. S. Novoselov, T. Tudorovskiy, I. V. Grigorieva, A. H. MacDonald, S. V. Morozov, K. Watanabe, T. Taniguchi, et al., Nature Physics **8**, 896 (2012).

[76] S. J. Haigh, A. Gholinia, R. Jalil, S. Romani, L. Britnell, D. C. Elias, K. S. Novoselov, L. A. Ponomarenko, A. K. Geim, and R. Gorbachev, Nature Materials **11**, 764 (2012).

[77] J. Zhang and E. Rossi, Phys. Rev. Lett. **111**, 086804 (2013).

[78] J. Lopes dos Santos, N. Peres, and A. Castro Neto, Phys. Rev. Lett. **99**, 256802 (2007).

[79] E. J. Mele, Phys. Rev. B **81**, 161405 (2010).

[80] S. Shallcross, S. Sharma, E. Kandelaki, and O. A. Pankratov, Phys. Rev. B **81**, 165105 (2010).

[81] E. Suárez Morell, J. D. Correa, P. Vargas, M. Pacheco, and Z. Barticevic, Phys. Rev. B **82**, 121407 (2010).

[82] R. Bistritzer and A. H. MacDonald, Phys. Rev. B **81**, 245412 (2010).

[83] J. Li, I. Martin, M. Buttiker, and A. F. Morpurgo, Nat. Phys. **7**, 42 (2011).

[84] E. J. Mele, Phys. Rev. B **84**, 235439 (2011).

[85] R. Bistritzer and A. H. MacDonald, Phys. Rev. B **84**, 035440 (2011).

[86] R. Bistritzer and A. H. MacDonald, Proc. National Acad. Sciences United States Am. **108**, 12233 (2011).

[87] E. Suárez Morell, P. Vargas, L. Chico, and L. Brey, Phys. Rev. B **84**, 195421 (2011).

[88] E. J. Mele, Journal of Physics D Applied Physics **45**, 154004 (2012).

[89] M. Kindermann and E. J. Mele, Phys. Rev. B **84**, 161406 (2011).

[90] A. Luican, G. Li, A. Reina, J. Kong, R. R. Nair, K. S. Novoselov, A. K. Geim, and E. Y. Andrei, Phys. Rev. Lett. **106**, 126802 (2011).

[91] W. Yan, M. Liu, R.-F. Dou, L. Meng, L. Feng, Z.-D. Chu, Y. Zhang, Z. Liu, J.-C. Nie, and L. He, Phys. Rev. Lett. **109**, 126801 (2012).

[92] J. D. Sanchez-Yamagishi, T. Taychatanapat, K. Watanabe, T. Taniguchi, A. Yacoby, and P. Jarillo-Herrero, Phys. Rev. Lett. **108**, 076601 (2012).

[93] P. San-Jose and E. Prada, Phys. Rev. B **88**, 121408 (2013), URL `http://link.aps.org/doi/10.1103/PhysRevB.88.121408`.

[94] C.-K. Lu and H. A. Fertig, Phys. Rev. B **89**, 085408 (2014), URL `http://link.aps.org/doi/10.1103/PhysRevB.89.085408`.

[95] J. Xue, J. Sanchez-Yamagishi, D. Bulmash, P. Jacquod, A. Deshpande, K. Watanabe, T. Taniguchi, P. Jarillo-Herrero, and B. J. LeRoy, Nature materials **10**, 282 (2011).

[96] M. Yankowitz, J. Xue, D. Cormode, J. D. Sanchez-Yamagishi, K. Watanabe, T. Taniguchi, P. Jarillo-Herrero, P. Jacquod, and B. J. Leroy, Nature Physics **8**, 382 (2012).

[97] L. A. Ponomarenko, R. V. Gorbachev, G. L. Yu, D. C. Elias, R. Jalil, A. A. Patel, A. Mishchenko, A. S. Mayorov, C. R. Woods, J. R. Wallbank, et al., Nature **497**, 594 (2013).

[98] B. Hunt, J. D. Sanchez-Yamagishi, A. F. Young, M. Yankowitz, B. J. LeRoy, K. Watanabe, T. Taniguchi, P. Moon, M. Koshino, P. Jarillo-Herrero, et al., Science **340**, 1427 (2013).

[99] C. R. Dean, L. Wang, P. Maher, C. Forsythe, F. Ghahari, Y. Gao, J. Katoch, M. Ishigami, P. Moon, M. Koshino, et al., Nature **497**, 598 (2013).

[100] M. Mucha-Kruczyński, J. R. Wallbank, and V. I. Fal'ko, Phys. Rev. B **88**, 205418 (2013), URL `http://link.aps.org/doi/10.1103/PhysRevB.88.205418`.

[101] K.-H. Jin and S.-H. Jhi, Phys. Rev. B **87**, 075442 (2013).

[102] L. Fu, Physical review letters **103**, 266801 (2009).

[103] J.-H. Chen, W. G. Cullen, C. Jang, M. S. Fuhrer, and E. D. Williams, Phys. Rev. Lett. **102**, 236805 (2009).

[104] J. G. Analytis, J. H. Chu, Y. L. Chen, F. Corredor, R. D. McDonald, Z. X. Shen, and I. R. Fisher, Phys. Rev. B **81**, 205407 (2010).

[105] D. Hsieh, Y. Xia, D. Qian, L. Wray, F. Meier, J. H. Dil, J. Osterwalder, L. Patthey, A. V. Fedorov, H. Lin, et al., Phys. Rev. Lett. **103**, 146401 (2009).

[106] H. Steinberg, D. R. Gardner, Y. S. Lee, and P. Jarillo-Herrero, Nano Letters **10**, 5032 (2010), `http://pubs.acs.org/optdoi/pdf/10.1021/nl1032183`, URL `http://pubs.acs.org/optdoi/abs/10.1021/nl1032183`.

[107] J. G. Checkelsky, Y. S. Hor, R. J. Cava, and N. P. Ong, Phys. Rev. Lett. **106**, 196801 (2011).

[108] Y. Zhang, K. He, C.-Z. Chang, C.-L. Song, L.-L. Wang, X. Chen, J.-F. Jia, Z. Fang, X. Dai, W.-Y. Shan, et al., Nature Physics **6**, 584 (2010).

[109] A. A. Taskin, S. Sasaki, K. Segawa, and Y. Ando, Phys. Rev. Lett. **109**, 066803 (2012).

[110] J. A. Hutasoit and T. D. Stanescu, Phys. Rev. B **84**, 085103 (2011).

[111] Note that the Dirac Hamiltonian of graphene in the sublattice basis has a phase factor on the off-diagonal terms to take into account a rotational transformation of coordinates due to the choice of the current BZ orientation.

[112] C. Triola, E. Rossi, and A. V. Balatsky, Phys. Rev. B **89**, 165309 (2014).

[113] M.-X. Wang, C. Liu, J.-P. Xu, F. Yang, L. Miao, M.-Y. Yao, C. L. Gao, C. Shen, X. Ma, X. Chen, et al., Science **336**, 52 (2012).

[114] T. Stanescu, J. Sau, R. Lutchyn, and S. Das Sarma, Phys. Rev. B **81**, 241310(R) (2010).

[115] T. Yokoyama, Phys. Rev. B **86**, 075410 (2012).

[116] A. Black-Schaffer and A. Balatsky, Phys. Rev. B **86**, 144506 (2012).

[117] A. Black-Schaffer and A. Balatsky, Phys. Rev. B **87**, 220506(R) (2013).

[118] L. Fu and C. Kane, Phys. Rev. Lett. **100**, 096407 (2008).

[119] Y. Tanaka, T. Yokoyama, and N. Nagaosa, Phys. Rev. Lett. **103**, 107002 (2009).

[120] J. Linder, Y. Tanaka, T. Yokoyama, A. Sudbø, and N. Nagaosa, Phys. Rev. Lett. **104**, 067001 (2010).

[121] J. Linder, Y. Tanaka, T. Yokoyama, A. Sudbø, and N. Nagaosa, Phys. Rev. B **81**, 184525 (2010).

[122] G. Koren, T. Kirzhner, Y. Kalcheim, and O. Millo, EPL (Europhysics Letters) **103**, 67010 (2013), URL `http://stacks.iop.org/0295-5075/103/i=6/a=67010`.

[123] V. L. Berezinskii, Pis' ma Zh. Eksp. Teor. Fiz. **20**, 628 (1974).

[124] A. Balatsky and E. Abrahams, Phys. Rev. B **45**, 13125 (1992).

[125] M. Eschrig and T. Löfwander, Nature Physics **4**, 138 (2008).

[126] J. Linder, T. Yokoyama, and A. Sudbø, Phys. Rev. B **77**, 174514 (2008).

[127] Y. Tanaka, Y. Tanuma, and A. Golubov, Phys. Rev. B **76**, 054522 (2007).

[128] J. Linder, T. Yokoyama, A. Sudbø, and M. Eschrig, Phys. Rev. Lett. **102**, 107008 (2009).

[129] J. Linder, A. Sudbø, T. Yokoyama, R. Grein, and M. Eschrig, Phys. Rev. B **81**, 214504 (2010).

[130] Y. Tanaka, M. Sato, and N. Nagaosa, J. Phys. Soc. Jpn. **81**, 011013 (2012).

[131] A. Millis, D. Rainer, and J. Sauls, Phys. Rev. B **38**, 4504 (1988).

[132] M. Eschrig, J. Kopu, J. Cuevas, and G. Schön, Phys. Rev. Lett. **90**, 137003 (2003).

[133] A. Cottet, D. Huertas-Hernando, W. Belzig, and Y. Nazarov, Phys. Rev. B **80**, 184511 (2009).

[134] T. Tokuyasu, J. Sauls, and D. Rainer, Phys. Rev. B **38**, 8823 (1988).

[135] A. Cottet and W. Belzig, Phys. Rev. B **72**, 180503(R) (2005).

[136] J. Kopu, M. Eschrig, J. Cuevas, and M. Fogelström, Phys. Rev. B **69**, 094501 (2004).

[137] F. Bergeret, A. Volkov, and K. Efetov, Phys. Rev. Lett. **86**, 4096 (2001).

[138] E. Demler, G. Arnold, and M. Beasley, Phys. Rev. B **55**, 15174 (1997).

[139] C. Triola, J.-X. Zhu, A. Migliori, and A. V. Balatsky, arXiv preprint arXiv:1501.03158 (2015).

[140] H. P. Dahal, Y. N. Joglekar, K. S. Bedell, and A. V. Balatsky, Phys. Rev. B **74**, 233405 (2006).

[141] E. V. Gorbar, V. P. Gusynin, V. A. Miransky, and I. A. Shovkovy, Phys. Rev. B **66**, 045108 (2002).

[142] O. V. Gamayun, E. V. Gorbar, and V. P. Gusynin, Phys. Rev. B **80**, 165429 (2009).

[143] O. V. Gamayun, E. V. Gorbar, and V. P. Gusynin, Phys. Rev. B **81**, 075429 (2010).

[144] J. E. Drut and T. A. Lähde, Phys. Rev. Lett. **102**, 026802 (2009).

[145] D. Khveshchenko, J. Phys.: Condens. Matter **21**, 075303 (2009).

[146] S. Ryu, C. Mudry, C.-Y. Hou, and C. Chamon, Phys. Rev. B **80**, 205319 (2009).

[147] D. C. Elias, R. V. Gorbachev, A. S. Mayorov, S. V. Morozov, A. A. Zhukov, P. Blake, L. A. Ponomarenko, I. V. Grigorieva, K. S. Novoselov, F. Guinea, et al., Nature Physics **7**, 701 (2011).

[148] H. Zhang, C.-X. Liu, X.-L. Qi, X. Dai, Z. Fang, and S.-C. Zhang, Nature Physics **5**, 438 (2009).

[149] P. Coleman, *Heavy fermions: Electrons at the edge of magnetism* (Wiley Online Library, 2007).

[150] M. Dzero, K. Sun, P. Coleman, and V. Galitski, Phys. Rev. B **85**, 045130 (2012).

[151] M. Dzero, K. Sun, V. Galitski, and P. Coleman, Phys. Rev. Lett. **104**, 106408 (2010).

[152] V. Alexandrov, M. Dzero, and P. Coleman, Phys. Rev. Lett. **111**, 226403 (2013).

[153] H. Weng, J. Zhao, Z. Wang, Z. Fang, and X. Dai, Phys. Rev. Lett. **112**, 016403 (2014).

[154] X. Deng, K. Haule, and G. Kotliar, Phys. Rev. Lett. **111**, 176404 (2013).

[155] M. Neupane, N. Alidoust, S. Xu, T. Kondo, Y. Ishida, D.-J. Kim, C. Liu, I. Belopolski, Y. Jo, T.-R. Chang, et al., Nature communications **4** (2013).

[156] N. Xu, P. Biswas, J. Dil, R. Dhaka, G. Landolt, S. Muff, C. Matt, X. Shi, N. Plumb, M. Radović, et al., Nature communications **5** (2014).

[157] J.-X. Zhu, B. Friedman, and C. Ting, Phys. Rev. B **59**, 3353 (1999).

VITA

Christopher Lawrence Charles Triola

Christopher Lawrence Charles Triola was born in Fredericksburg Virginia in 1984. From a young age he knew he wanted to be a scientist but didn't find his passion for Physics until he went to college. He spent his first summer at William and Mary working with Marc Sher on the astrophysical consequences of neutrino-philic two-Higgs doublet models. This work was subsequently published in Physical Review D. The following year he took his first course on condensed matter physics to satisfy an elective and found it so interesting that he began working with his professor, Enrico Rossi, on the theoretical properties of chiral two-dimensional systems. In the summer of 2013 he traveled to Los Alamos, New Mexico for the waters. However, he was misinformed. Fortunately, that summer he began working with Alexander (Sasha) Balatsky at Los Alamos National Laboratory studying the effect of a spin-active interface on proximity-induced superconductivity in topological insulators. The next summer Christopher returned to Los Alamos to study the possibility of Coulomb-driven ordered states on the surfaces of topological Kondo insulators. During the Fall of 2014, Christopher was selected as a postdoctoral research fellow at the Nordic Institute for Theoretical Physics in Stockholm, Sweden, a position to start in March 2015. Thus, he has been given a few short months to prepare a dissertation and to defend it before he embarks on his first journey outside of his home country.